Supplemental Material
Flow and structure in nonequilibrium Brownian many-body systems

Daniel de las Heras[1] and Matthias Schmidt[1]

[1] *Theoretische Physik II, Physikalisches Institut, Universität Bayreuth, D-95440 Bayreuth, Germany*

(Dated: May 28, 2020)

We show here simulation results (Brownian dynamics) and theoretical predictions (power functional theory) of the superadiabatic forces that occur in eight different steady states of a model microscopic fluid interacting via a repulsive pair potential. For each steady state we impose the specific spatial form of the velocity and the density profiles using the custom flow method [1]. This Supplemental Material is organized as follows. In Sec. I we define the particle model, and give details about the simulation. In Sec. II we present the power functional theory that we use to describe the simulation data. In Sec. III we show the results for different steady states and include a comparison between results from simulation and theory for all types of superadiabatic forces. Finally, in Sec. IV we discuss possible finite size effects and conclude.

I. SIMULATIONS

A. Particle model

We study a two-dimensional system of interacting particles in a square simulation box with periodic boundary conditions. The particles interact via the Weeks-Chandler-Anderson potential [2], i.e. a purely repulsive, truncated-and-shifted Lennard-Jones (LJ) pair potential given by

$$\phi(r) = \begin{cases} 4\epsilon\left[\left(\frac{\sigma}{r}\right)^{12} - \left(\frac{\sigma}{r}\right)^{6} + \frac{1}{4}\right] & \text{if } r < r_c \\ 0 & \text{otherwise,} \end{cases} \tag{1}$$

where σ and ϵ are the length and energy scales, respectively, and $r_c/\sigma = 2^{1/6}$ is the cutoff distance which corresponds to the position of the minimum of the LJ potential. Time is measured in units of $\tau = \sigma^2\gamma/\epsilon$ with γ being the friction coefficient. In all cases considered below we set the number of particles to $N = 5$, and we use a square simulation box of side length $H/\sigma = 5$ (the average density is therefore $\rho_0\sigma^2 = 0.20$). The temperature is set to $k_BT/\epsilon = 0.5$.

We use a reduced number of particles to be able to sample for very long times and obtain high quality force profiles. We note however that our previous works [3] show that even a system with only two particles is enough to observe the physically correct behaviour of superadiabatic forces.

B. Brownian Dynamics simulations

The equation of motion for the $i-$th particle is

$$\gamma\frac{d\mathbf{r}_i(t)}{dt} = -\nabla_i u(\mathbf{r}^N) + \mathbf{f}_{\text{ext}}(\mathbf{r}_i, t) + \boldsymbol{\chi}_i(t), \tag{2}$$

where $u = \sum_i \sum_{i<j} \phi(r_{ij})$ is the total potential energy of microstate $\mathbf{r}^N = [\mathbf{r}_1, ..., \mathbf{r}_N]$ with r_{ij} being the distance between particles i and j. The external force is $\mathbf{f}_{\text{ext}}$ and $\boldsymbol{\chi}_i$ is a Gaussian random force acting on particle i. Time discretization of equation (2) using the standard Euler algorithm results in

$$\mathbf{r}_i(t+\Delta t) = \mathbf{r}_i(t) + \frac{\Delta t}{\gamma}\left[-\nabla_i u(\mathbf{r}^N) + \mathbf{f}_{\text{ext}}(\mathbf{r}_i, t)\right] + \boldsymbol{\eta}_i(t), \tag{3}$$

with $\boldsymbol{\eta}_i$ a delta-correlated Gaussian random displacement with standard deviation $\sqrt{2\Delta t k_BT/\gamma}$. We integrate the equations of motion (3) using a time step $\Delta t/\tau = 10^{-4}$.

To find the external force fields that produce the forward and the reverse steady states, as well as the external force in the adiabatic (equilibrium) state we use the custom flow method [1]. This method finds iteratively the external force field that is required to produce the prescribed velocity and density profiles. We briefly reproduce here the main steps of the method for steady states and refer the reader to Ref. [1] for a detailed description of its implementation and also of several different methods that can be used to correctly sample the current and the velocity profiles (see the Appendix of Ref. [1]). The exact force balance equation in an overdamped Brownian system is

$$\gamma\mathbf{v} = \mathbf{f}_{\text{id}} + \mathbf{f}_{\text{int}} + \mathbf{f}_{\text{ext}}, \tag{4}$$

where the ideal diffusion is known explicitly $\mathbf{f}_{\text{id}} = -k_BT\nabla\ln\rho$. To find the external force $\mathbf{f}_{\text{ext}}$ required to produce target velocity ($\mathbf{v}$) and density (ρ) profiles in steady states, we first solve the above equation for $\mathbf{f}_{\text{ext}}$,

$$\mathbf{f}_{\text{ext}} = \gamma\mathbf{v} + k_BT\nabla\ln\rho - \mathbf{f}_{\text{int}}. \tag{5}$$

Both ρ and $\mathbf{v}$ are known for a given (target) steady state. Hence, the internal force field $\mathbf{f}_{\text{int}}$ is the only unknown field in the right-hand side of Eq. (5). We find $\mathbf{f}_{\text{ext}}$ iteratively. In iteration k the external force is

$$\mathbf{f}_{\text{ext}}^{(k)} = \gamma\mathbf{v} + k_BT\nabla\ln\rho - \mathbf{f}_{\text{int}}^{(k-1)}, \tag{6}$$

with $\mathbf{f}_{\text{int}}^{(k-1)} = \mathbf{F}_{\text{int}}^{(k-1)}/\rho$ and $\mathbf{F}_{\text{int}}^{(k-1)}$ the internal force density sampled at the previous iteration (i.e. under the

influence of the external force $\mathbf{f}_{\rm ext}^{(k-1)}$). To initialize the iterative scheme we set at $k=0$ the external force in an ideal gas, i.e.

$$\mathbf{f}_{\rm ext}^{(0)} = \gamma \mathbf{v} + k_B T \nabla \ln \rho. \tag{7}$$

We then run a simulation with $\mathbf{f}_{\rm ext}^{(0)}$ and sample $\mathbf{f}_{\rm int}^{(0)}$ which goes then into Eq. (6) to find an expression for the external force at the next iteration $k=1$. The iterative process terminates when the external force is close enough to that required to impose the target fields, which can be easily checked by sampling at each iteration the velocity and the density profiles and comparing them with the target ones.

For each type of flow and for each state (adiabatic, forward, and reverse) about 50 iterations are enough to find the external forces. The total sampling time in the first iteration is set to 10^3 τ and it linearly increases in each iteration until it reaches $5\cdot 10^6$ τ in the last iteration. Finally, we average over at least 100 of such runs such that the results shown here represent an average over at least $5\cdot 10^8$ τ for each state (adiabatic, forward, and reverse). Together with the reduced number of particles, these ultralong simulation runs enable us to obtain quasi-exact reference data with two-dimensional space resolution.

II. POWER FUNCTIONAL THEORY

Within the formalism of density functional theory [4], the adiabatic force field ($\mathbf{f}_{\rm ad}$) is given exactly as

$$\mathbf{f}_{\rm ad}(\mathbf{r},t) = -\nabla \frac{\delta F_{\rm exc}[\rho]}{\delta \rho(\mathbf{r},t)}, \tag{8}$$

where $F_{\rm exc}$ is the excess (over ideal gas) intrinsic free energy functional. The adiabatic force field is an equilibrium-like force, since it only depends on the density distribution for a given type of interparticle interaction potential. Within the formally exact power functional theory (PFT) [5], the superadiabatic force field ($\mathbf{f}_{\rm sup}$) is generated as the functional derivative of the excess power functional $P_t^{\rm exc}$ via

$$\mathbf{f}_{\rm sup}(\mathbf{r},t) = -\frac{\delta P_t^{\rm exc}}{\delta \mathbf{J}(\mathbf{r},t)} = -\frac{1}{\rho}\frac{\delta P_t^{\rm exc}}{\delta \mathbf{v}(\mathbf{r},t)}, \tag{9}$$

where $P_t^{\rm exc}$ and consequently $\mathbf{f}_{\rm sup}$ are functionals of both the density and the current profile. We express the excess power functional as a series expansion in powers of the velocity $\mathbf{v}$ and the density ρ. The terms that are even in $\mathbf{v}$ generate superadiabatic flow forces, which are odd in $\mathbf{v}$, and hence reverse their direction under flow reversal. Note that the functional derivative (9) reduces by one the order in powers of $\mathbf{v}$ of the superadiabatic forces $\mathbf{f}_{\rm sup}$ as compared to the order that appears in $P_t^{\rm exc}$. Terms of the expansion of $P_t^{\rm exc}$ that are odd in powers of $\mathbf{v}$ generate via Eq. (9) superadiabatic structural forces that remain unchanged under flow reversal, and are of even power in $\mathbf{v}$.

It is therefore natural to split the excess power functional into flow ($P_t^{\rm flow}$) and structural ($P_t^{\rm str}$) contributions:

$$P_t^{\rm exc} = P_t^{\rm flow} + P_t^{\rm str}, \tag{10}$$

where $P_t^{\rm flow}$ contains even powers of $\mathbf{v}$ and $P_t^{\rm str}$ contains odd powers of $\mathbf{v}$.

Flow superadiabatic contributions. We use the following second and fourth order terms (in powers of $\mathbf{v}$) to describe the flow contributions of the superadiabatic force field:

$$P_t^{\rm flow} =$$

$$f_1 \int d\mathbf{r}\rho^2(\nabla\cdot\mathbf{v})^2 + \tag{11}$$

$$f_2 \int d\mathbf{r}\rho^2(\nabla_i v_j)(\nabla_i v_j) + \tag{12}$$

$$f_3 \int d\mathbf{r}\rho^2(\nabla_i v_j)(\nabla_j v_i) + \tag{13}$$

$$f_4 \int d\mathbf{r}\int_0^t dt' K(t-t')\rho^4(\nabla_i v_k')(\nabla_j v_k')v_i v_j + \tag{14}$$

$$f_5 \int d\mathbf{r}\int_0^{t'} dt K(t-t')\rho^4[\nabla\times\nabla\times\mathbf{v}']^2\mathbf{v}^2. \tag{15}$$

where we have omitted the spatio-temporal dependence of ρ and $\mathbf{v}$ to simplify the notation and have used the Einstein summation convention over repeated indices. ∇_i indicates the derivative with respect to the i-coordinate, and v_i is the i-component of the velocity. The coefficients f_i with $i=1,...,5$ are flow transport coefficients that depends on e.g. the interparticle potentials. They can be expressed as functional derivatives of the excess power functional with respect to the velocity gradient. Here we adjust the transport coefficients to reproduce the magnitude of the superadiabatic response obtained in the simulations (note that the theory reproduces the complete shape of the superadiabatic response, only the magnitude is unknown). Here, $\mathbf{v}'=\mathbf{v}(\mathbf{r},t')$ and $K(t-t')$ is a temporal kernel normalized such that

$$\lim_{t\to\infty}\int_0^t dt' K(t-t') = 1. \tag{16}$$

The precise form of the temporal kernel (not studied here) is relevant in full non-equilibrium, but not in steady state. The only effect of the primed terms in Eqs. (14) and (15) is that the functional derivative required to obtain the superadiabatic force, see Eq. (9), does not act on them. The term $(\nabla_i v_k')(\nabla_j v_k')v_i v_j$ in the integrand of Eqs. (14) results from the contraction $\mathsf{N}_{ijklmn}(\nabla_i v_j')(\nabla_k v_l')v_m v_n$, with N being an isotropic tensor of rank six. The superadiabatic flow forces $\mathbf{f}_{\rm flow}$ are generated from $P_t^{\rm flow}$ via functional differentiation, cf. Eq. (9).

Flow #	f_1^*	f_2^*	f_3^*	f_4^*	f_5^*
1		0.038		0.41	
2		0.046	0.045		
3		0.046		0.13	-0.080
4		0.045	0.046		
5	0.031	0.049	0.049		
6	0.032	0.048	0.034		
7	0.034	0.047	0.047		
8	0.041	0.041	0.031		

Not active Not required

FIG. 1. Scaled value of the flow coefficients ${f_\alpha}^*$, $\alpha = 1, .., 4$ for the different flows considered here. The values have been obtained by adjusting the theoretical flow force to the flow force in BD simulations. The scale factors are: ${f_i}^* = f_i/\epsilon\sigma^2\tau$ for $i = 1, 2, 3, ,$ ${f_4}^* = f_4/\epsilon\sigma^4\tau^3$, and ${f_5}^* = f_5\epsilon\sigma^6\tau^3$. The blue cells indicate the corresponding flow force vanishes due to the characteristics of the flow ($\mathbf{v}$ and ρ). The green cells (high order terms in $\mathbf{v}$) indicate that even though the corresponding flow force does not vanish, it is not necessary to include the high order term in order to reach an excellent agreement with BD simulations since the low order terms already reproduce the data.

The terms that are of second order in velocity, Eqs. (11), (12) and (13), are a simplification of the more general second order excess power functional based on the velocity-gradient form given by [6] as

$$P_t^{\text{flow}} = \int d\mathbf{r} \int d\mathbf{r}' \int_0^t dt' \rho(\mathbf{r}, t) \nabla \mathbf{v}(\mathbf{r}, t) : \mathsf{M}(\mathbf{r} - \mathbf{r}', t - t') : \nabla \mathbf{v}(\mathbf{r}', t') \rho(\mathbf{r}', t'), \quad (17)$$

where the kernel $\mathsf{M}(\mathbf{r}, t)$ is a fourth-rank tensor that carries physical units of energy, and in general depends functionally on the density profile. Here, the state of the system is assumed to be known at the initial time $t = 0$, and the colon indicates a double tensor contraction.

As the excess power must be invariant under arbitrary rotations, the tensor M needs to be isotropic and hence its components are given by

$$\mathsf{M}_{ijkl} = \mathsf{m}_1 \delta_{ij}\delta_{kl} + \mathsf{m}_2 \delta_{ik}\delta_{jl} + \mathsf{m}_3 \delta_{il}\delta_{jk}, \quad (18)$$

where δ_{ij} etc indicates the Kronecker delta, and $\mathsf{m}_\alpha = \mathsf{m}_\alpha(\mathbf{r} - \mathbf{r}', t - t')$ with $\alpha = 1, 2, 3$ depend on the interparticle potential and may also depend functionally on the density profile. Here, we limit ourselves to steady states, and hence use a local approximation in space and in time for the memory functions

$$\mathsf{m}_\alpha(\mathbf{r} - \mathbf{r}', t - t') = \mathsf{f}_\alpha \delta(\mathbf{r} - \mathbf{r}')\delta(t - t'), \quad (19)$$

where f_α are constants, the values of which are adjusted to match the simulation data. For full time-dependent situations memory effects are in place and the time dependence of m_α might be relevant [3, 6]. Insertion of Eq. (18) into Eq. (17) results in the first three contributions of P_t^{flow} given in Eqs. (11), (12) and (13). The superadiabatic forces generated by these second order in $\mathbf{v}$ contributions, cf. Eqs. (11), (12) and (13), are a very good approximation of the superadiabatic flow forces in most cases considered here. However, fourth order isotropic terms, cf. Eqs. (14) and (15), are required to have a proper description of the flow forces in two of the steady-states studied below (flows 1 and 3).

The flow transport coefficients, f_α with $\alpha = 1, ..., 5$, are obtained by adjusting the predicted flow superadiabatic force to the simulation data for each specific flow. The results for the flow transport coefficients are presented in Fig. 1. We find that the values of each transport coefficient are similar across the different flows. Moreover, the data clearly suggests the equality $f_2 = f_3$ indicating that Eqs. (12) and (13) can be combined using the square of the curl of the velocity field [6].

Out of eight different steady states considered here, only the flows number 1 and 3 (described below) require the inclusion of the higher order terms in order to achieve excellent agreement with simulation data. In flow 1 the inclusion of (14) has a big effect on the superadiabatic flow force parallel to the flow, $\mathbf{f}_{\text{flow}}^{||}$, predicted by PFT, see Fig. 11 panels (a3) and (a4). Without (14), the predicted $\mathbf{f}_{\text{flow}}^{||}$ is only a sine wave opposing the flow and does not reproduce the complex secondary structure shown in the data. Moreover, the perpendicular flow force $\mathbf{f}_{\text{flow}}^{\perp}$ presented in Fig. 11 panels (b3) and (b4) is completely generated by this higher other term and therefore cannot be described within the conventional Navier-Stokes viscosity form. The higher order terms are also required to reproduce in theory the y-component of the superadiabatic flow force $\mathbf{f}_{\text{flow}} \cdot \hat{\mathbf{y}}$ of flow 3, which otherwise would vanish due to an exact cancellation between the parallel and the perpendicular components, see Fig. 5(e2).

Structural superadiabatic contributions. Structural superadiabatic forces are generated by terms of the excess power that are odd in powers of the velocity. The superadiabatic forces generated by such terms are even in powers of the velocity and hence remain unchanged upon flow reversal. Based on our simulation data and using a spatially local approximation for the kernels, we propose the following terms of the expansion of P_t^{exc} to generate the structural components of the superadiabatic

Flow #	s_1^*	s_2^*	s_3^*	s_4^*	s_5^*	s_6^*	s_7^*	s_8^*	s_9^*
1		0.016	-0.017	0.0091		-0.040	-0.025	-0.029	-0.043
2		-0.062	0.16	0.76		-0.057	-0.067	0.021	0.032
3		0.018	-0.045	0.036		-0.028	-0.028		
4		-0.040	-0.25	-0.19		-0.0078	-0.0078		
5	0.60	-0.035	-0.39	-0.60	-0.006	0.056	0.033	0.038	-0.14
6	0.48	0.21	-0.48	-0.38	-0.10	-0.0061	-0.0071	-0.10	-0.010
7	-0.060		-0.060	-0.030	-0.017				
8	-0.094		-0.094						

Not active / Not required

FIG. 2. Scaled value of the structural coefficients for the different flows considered here. The values have been obtained by adjusting the theoretical structural force to the structural force in BD simulations. The scale factors are: $s_i{}^* = s_i/\epsilon\sigma^2\tau^2$, for $i = 1, 2, 3, 4$ and $s_i{}^* = s_i/\epsilon\sigma^4\tau^2$ for $i = 5, 6, 7, 8, 9$. The blue cells indicate that either the corresponding structural force vanishes due to the characteristics of the flow or that the term was not included in order to compare with BD simulations.

force field:

$$P_t^{\rm str} =$$

$$s_1 \int d\mathbf{r} \int_0^t dt' K(t-t')\rho^3(\nabla\cdot\mathbf{v}')\mathbf{v}^2 + \tag{20}$$

$$s_2 \int d\mathbf{r} \int_0^t dt' K(t-t')\rho^3(\nabla_i v_j')v_i v_j + \tag{21}$$

$$s_3 \int d\mathbf{r} \int_0^t dt' K(t-t')\rho^3(\nabla\cdot\mathbf{v})\mathbf{v}'^2 + \tag{22}$$

$$s_4 \int d\mathbf{r} \int_0^t dt' K(t-t')\rho^3(\nabla_i v_j)v_i' v_j' + \tag{23}$$

$$s_5 \int d\mathbf{r}\rho^3(\nabla\cdot\mathbf{v})^3 + \tag{24}$$

$$s_6 \int d\mathbf{r}\rho^3(\nabla_i v_k)(\nabla_j v_k)(\nabla_i v_j) + \tag{25}$$

$$s_7 \int d\mathbf{r}\rho^3(\nabla\cdot\mathbf{v})(\nabla_i v_j)(\nabla_i v_j) + \tag{26}$$

$$s_8 \int d\mathbf{r}\rho^3(\nabla\cdot\mathbf{v})(\nabla_i v_j)(\nabla_j v_i) + \tag{27}$$

$$s_9 \int d\mathbf{r}\rho^3(\nabla_i v_j)(\nabla_k v_i)(\nabla_j v_k). \tag{28}$$

All terms (20)–(28) are third order in the velocity field and we assume the temporal kernel K to be the same as in the above case of the flow forces since we are only interested in steady states for which the functional form of K does not play a relevant role. In full nonequilibrium situations each contribution to $P_t^{\rm exc}$ might posses different temporal kernels. Here, as before, $\mathbf{v}' = \mathbf{v}(\mathbf{r}, t')$. The first four contributions to $P_t^{\rm str}$, Eqs. (20)–(23), result from the only two isotropic terms of the contractions $\nabla\mathbf{v}' : \mathsf{L} : \mathbf{v}\mathbf{v}$, and $\nabla\mathbf{v} : \mathsf{P} : \mathbf{v}'\mathbf{v}'$ with L and P isotropic tensors of rank four. The further terms, Eqs. (24) to (28), are constructed with the isotropic combinations of $\mathsf{Q}_{ijkmnl}(\nabla_i v_j)(\nabla_k v_m)(\nabla_n v_l)$, with Q an isotropic tensor of rank six. There exist 15 isotropic tensors of six rank that result in 5 five different contributions to $P_{\rm exc}^{\rm 3s}$, see Eqs. (24)–(28).

The parameters s_α^s with $\alpha = 1, ..., 9$ that best reproduce the simulation data are shown in Fig. 2. As we demonstrate below, the predicted structural forces are in excellent agreement with those measured in computer simulations. However, in contrast to the flow transport coefficients, the structural transport coefficients (Fig. 2) show a significant variation across different flows. The reason is potentially the presence of further hidden symmetry properties of $P_t^{\rm exc}$ that impose relations between the structural transport coefficients. This constitutes the subject of future work.

III. STEADY STATES

We consider eight different types of flow in steady state. The results are shown in two sets of figures. The first set, Figs. 3 to 10, displays for each flow the velocity and density profiles, $\mathbf{v}(\mathbf{r})$ and $\rho(\mathbf{r})$, the external force field in the forward and reverse states, $\mathbf{f}_{\rm ext}(\mathbf{r})$ and $\mathbf{f}'_{\rm ext}$, the diffusive force field, $\mathbf{f}_{\rm id}(\mathbf{r})$, the adiabatic force field, $\mathbf{f}_{\rm ad}(\mathbf{r})$, the complete superadiabatic force field, $\mathbf{f}_{\rm sup}(\mathbf{r})$, and the splitting into flow and structural components, $\mathbf{f}_{\rm flow}(\mathbf{r})$ and $\mathbf{f}_{\rm sup}(\mathbf{r})$. The second set of figures, Figs. 11 to 18 shows the full splitting of the superadiabatic force field into the four different contributions, $\mathbf{f}_{\rm flow}^{||}(\mathbf{r})$, $\mathbf{f}_{\rm flow}^{\perp}(\mathbf{r})$, $\mathbf{f}_{\rm str}^{||}(\mathbf{r})$ and $\mathbf{f}_{\rm str}^{\perp}(\mathbf{r})$, along with plots of the divergence and curl of the velocity field, $\nabla\cdot\mathbf{v}$ and $\nabla\times\mathbf{v}$, and the current profiles $\mathbf{J}(\mathbf{r})$.

Flow 1

This is the flow that is shown in the main text: a generalization of Kolmogorov flow in which the velocity profile is a pure sine wave for each Cartesian component and the density is homogeneous:

$$\begin{aligned} v_x(\mathbf{r}) &= v_0 \sin(2\pi y/H) \\ v_y(\mathbf{r}) &= v_0 \sin(2\pi x/H) \\ \rho(\mathbf{r}) &= \rho_0, \end{aligned} \tag{29}$$

with $v_0\tau/\sigma = 1.0$. The velocity profile is divergence-free and it has nonvanishing curl,

$$\nabla \cdot \mathbf{v} = 0, \quad \nabla \times \mathbf{v} \neq 0. \tag{30}$$

Flow and force profiles are shown in Fig. 3. A full split of the superadiabatic forces is shown in Fig. 11 together with the current profile, and the divergence and the curl of the velocity field.

Due to the symmetry of the flow, the x- and y-components of all forces are related via an anticlockwise rotation by 90° followed by a reflection at the y-axis. As the density is constant, the ideal diffusion and the adiabatic force field vanish. The internal force field is hence purely superadiabatic. The flow force perpendicular to the velocity field, Fig. 11 panels (b1) and (b2), is particularly complex and it requires high order terms in the expansion of P_t^{flow} in order to reproduce it. As shown below, the imposition of a constant density profile is the main reason behind the complexity of $f_{\text{flow}}^{\perp}$.

Flow 2

This steady state has the same velocity profile as flow 1 but it possesses an inhomogeneous density profile:

$$\begin{aligned} v_x(\mathbf{r}) &= v_0 \sin(2\pi y/H) \\ v_y(\mathbf{r}) &= v_0 \sin(2\pi x/H) \\ \rho(\mathbf{r}) &= \rho_0 \left\{1 + \rho_1 \left[\cos(2\pi x/H) - \cos(2\pi y/H)\right]\right\}, \end{aligned} \tag{31}$$

with $v_0\tau/\sigma = 1.0$, and $\rho_1\sigma^2 = 0.45$. Therefore, for this velocity field

$$\nabla \cdot \mathbf{v} = 0, \;\; \nabla \times \mathbf{v} \neq 0. \tag{32}$$

Flow and force profiles are shown in Fig. 4. A full split of the superadiabatic forces is shown in Fig. 12 together with the current profile, and the divergence and the curl of the velocity field.

Due to the strong density modulation, see Fig. 4(a3), the particles primarily wind around only two points of the velocity field as compared to four such center points in the previous flow 1, compare illustrative particle trajectories in Figs. 3(a4) and 4(a4). For visualization purposes the diffusive term (Brownian motion) has not been included in the equation of motion when calculating the illustrative trajectories shown in panels (a4) of Figs. 3 to 10.

The ideal diffusion and the adiabatic force field are strongly inhomogeneous as a consequence of the density modulation. The superadiabatic force field resembles that of flow 1 but it is strongly influenced by the density modulation. It is particularly interesting to compare the perpendicular flow component $\mathbf{f}_{\text{flow}}^{\perp}$ in both flows 1 and 2, since they are completely different, see Figs. 11(b1-b2) and 12(b1-b2). In flow 2, the compressible form of the Navier-Stokes equations gives a good description of $\mathbf{f}_{\text{flow}}^{\perp}$. However, in flow 1 the density is constant and the Navier-Stokes equations predict a vanishing flow force perpendicular to the velocity field. The observed force fields $\mathbf{f}_{\text{flow}}^{\perp}$ in flows 1 and 2 are therefore generated by different mechanisms. In flow 2 the second order terms of the expansion of P_t^{exc} generate $\mathbf{f}_{\text{flow}}^{\perp}$, see Eqs. (12) and (13). In contrast, in flow 1 the superadiabatic forces $\mathbf{f}_{\text{flow}}^{\perp}$ generated by Eqs. (12) and (13) vanish due to the constant density profile. Instead, $\mathbf{f}_{\text{flow}}^{\perp}$ is generated by the higher order term given in Eq. (14).

Flow 3

Next we consider a steady state with constant density profile, a pure sine wave for one component of the velocity and a constant value for the other component:

$$\begin{aligned} v_x(\mathbf{r}) &= v_0 \sin(2\pi y/H) \\ v_y(\mathbf{r}) &= v_0 \\ \rho(\mathbf{r}) &= \rho_0, \end{aligned} \tag{33}$$

with $v_0\tau/\sigma = 1.0$. Therefore, for this flow again

$$\nabla \cdot \mathbf{v} = 0, \;\; \nabla \times \mathbf{v} \neq 0. \tag{34}$$

Flow and force profiles are shown in Fig. 5. A full split of the superadiabatic forces is shown in Fig. 13 together with the current profile, and the divergence and the curl of the velocity field.

The ideal diffusion and the adiabatic force field vanish and hence the internal force is of superadiabatic origin. All forces depend only on the $x-$coordinate due to the characteristics of $\mathbf{v}$ and ρ. The velocity profile is a Kolmogorov flow (inhomogeneous shear) for the $x-$component of the velocity and a constant value for the $y-$component. The steady state is related to the first example discussed in the main text (figure 1), with two important differences: (i) there is a constant velocity in the direction orthogonal to the shear flow, and (ii) the density is homogeneous by construction. Structural forces (migration forces) appear in the direction perpendicular to the shear flow, Fig. 5(f2), and are precisely balanced by the external force (the density is imposed to be homogeneous). In the direction of the shear flow the superadiabatic force is dominated by a flow component of viscous type, Fig. 5(e1). Remarkably, there exist flow superadiabatic forces in the direction perpendicular to the shear flow, Fig. 5(e2), and structural forces in the direction of the shear flow, Fig. 5(f1). These two contributions to the superadiabatic force field are not present if the constant velocity in the direction perpendicular to the shear flow vanishes (figure 1 of the main text).

Flow 4

As in the case of flows 1 and 2, we consider again the effect of the density profile on the superadiabatic forces by studying a steady-state with the same velocity profile as that in flow number 3 but with an inhomogeneous

density profile. The flow is characterised by the following velocity and density profiles

$$\begin{aligned} v_x(\mathbf{r}) &= v_0 \sin(2\pi y/H) \\ v_y(\mathbf{r}) &= v_0 \\ \rho(\mathbf{r}) &= \rho_0 \left\{1 + \rho_1 \cos\left[2\pi x/H - \cos(2\pi y/H)\right]\right\}, \end{aligned} \tag{35}$$

with $v_0\tau/\sigma = 1.0$, and $\rho_1\sigma^2 = 0.5$. Hence, as in previous cases we find for this flow

$$\nabla \cdot \mathbf{v} = 0, \;\; \nabla \times \mathbf{v} \neq 0. \tag{36}$$

Flow and force profiles are shown in Fig. 6. A full split of the superadiabatic forces is shown in Fig. 14 together with the current profile, and the divergence and the curl of the velocity field.

A comparison between the superadiabatic forces that occur in flows 3 and 4 is particularly useful to understand how the inhomogeneities in the density profile affect the superadiabatic forces. Compare e.g. the striking difference between the y-components of the superadiabatic flow forces of flows 3 and 4, see Figs. 5 and 6 panels (d2),(e2), and (f2).

Flow 5

We next focus on a potential (curl-free) flow. The flow is characterised by the following velocity and density profiles:

$$\begin{aligned} v_x(\mathbf{r}) &= v_0 \left(1 + v_1 \sin(2\pi x/H)\right) \\ v_y(\mathbf{r}) &= v_0 \left(1 + v_1 \sin(2\pi y/H)\right) \\ \rho(\mathbf{r}) &= \rho^* / \left(v_x(\mathbf{r}) v_y(\mathbf{r})\right), \end{aligned} \tag{37}$$

with $v_0\tau/\sigma = 1.0$, $v_1\tau/\sigma = 0.3$, and ρ^* a constant such that $\int d\mathbf{r}\rho(\mathbf{r}) = N$. Therefore, we obtain for this flow

$$\nabla \cdot \mathbf{v} \neq 0, \;\; \nabla \times \mathbf{v} = 0. \tag{38}$$

This is the first example shown here of a potential flow, that is, the divergence of the flow does not vanish and the flow is curl-free. Flow and force profiles are shown in Fig. 7. A full split of the superadiabatic forces is shown in Fig. 15 together with the current profile, and the divergence and the curl of the velocity field.

The superadiabatic forces are dominated by flow components, Fig. 7(e1-e2). Interestingly, the structural components, Fig. 7(f1-f2), are mostly aligned with the adiabatic forces, Fig. 7(c3-c4), instead of opposing them as it was the case in previous examples with inhomogeneous density profiles (flows 2 and 4).

Flow 6

We continue to increase the complexity of the nonequilibrium situation under consideration and consider a flow that is characterised by the following velocity and density profiles:

$$\begin{aligned} v_x(\mathbf{r}) &= v_0 \sin(2\pi y/H) \\ v_y(\mathbf{r}) &= v_0 \left(1 + v_1 \cos(2\pi y/H)\right) \\ \rho(\mathbf{r}) &= \rho^* / v_y(\mathbf{r}), \end{aligned} \tag{39}$$

with $v_0\tau/\sigma = 1.0$, $v_1\tau/\sigma = 0.5$, and ρ^* a constant such that $\int d\mathbf{r}\rho(\mathbf{r}) = N$. For this flow neither the divergence nor the curl vanish

$$\nabla \cdot \mathbf{v} \neq 0, \;\; \nabla \times \mathbf{v} \neq 0. \tag{40}$$

Flow and force profiles are shown in Fig. 8. A full split of the superadiabatic forces is shown in Fig. 16 together with the current profile, and the divergence and the curl of the velocity field.

An interesting observation for this flow is the partial cancellation that occurs between the parallel and perpendicular $x-$components of the structural superadiabatic force. Compare $\mathbf{f}_{\rm str} \cdot \hat{\mathbf{x}}$ in Fig. 8(f1) with $\mathbf{f}^{||}_{\rm str} \cdot \hat{\mathbf{x}}$ and $\mathbf{f}^{\perp}_{\rm str} \cdot \hat{\mathbf{x}}$ in Figs. 16(c1-c2). This highlights the importance of the splitting of the superadiabatic forces according to their direction.

Flow 7

We next consider a velocity profile in which one Cartesian component vanishes. The flow is characterised by the following velocity and density profiles:

$$\begin{aligned} v_x(\mathbf{r}) &= v_0(1 + 0.5 \sin(2\pi x/H)) \\ v_y(\mathbf{r}) &= 0 \\ \rho(\mathbf{r}) &= \rho^*/v_x(\mathbf{r}), \end{aligned} \tag{41}$$

with $v_0\tau/\sigma = 1.0$, and ρ^* a constant such that $\int d\mathbf{r}\rho(\mathbf{r}) = N$. The steady state is effectively one-dimensional since no dependence on the $y-$coordinate appears in either $\mathbf{v}$ or ρ. The velocity profile satisfies

$$\nabla \cdot \mathbf{v} \neq 0, \;\; , \nabla \times \mathbf{v} = 0. \tag{42}$$

Flow and force profiles are shown in Fig. 9. A full split of the superadiabatic forces is shown in Fig. 17 together with the current profile, and the divergence and the curl of the velocity field.

The $\hat{\mathbf{y}}-$components of all forces vanish, as do as the complete superadiabatic forces perpendicular to the flow $\mathbf{f}^{\perp}_{\rm flow}$ and $\mathbf{f}^{\perp}_{\rm str}$. The flow component, Fig. 9(e1), dominates the superadiabatic force, Fig. 9(d1). However, the structural component, Fig. 9(f1), is far from being negligible and it plays a different role than the flow component by aligning with the adiabatic and diffusive fields, Figs. 9(c1,c3).

Flow 8

The last steady state shares the velocity profile with flow 7. The density profile is, however, different and it depends on both spatial coordinates which, as we see below, has a strong influence on the superadiabatic forces. The flow is characterised by:

$$\begin{aligned} v_x(\mathbf{r}) &= v_0(1 + 0.5 \sin(2\pi x/H)) \\ v_y(\mathbf{r}) &= 0 \\ \rho(\mathbf{r}) &= \rho^*(1 + 0.5 \sin(2\pi y/H)/v_x(\mathbf{r}), \end{aligned} \tag{43}$$

with $v_0\tau/\sigma = 1.0$, and ρ^* a constant such that $\int d\mathbf{r}\rho(\mathbf{r}) = N$. Therefore, for this flow

$$\nabla \cdot \mathbf{v} \neq 0, \quad \nabla \times \mathbf{v} = 0. \tag{44}$$

Flow and force profiles are shown in Fig. 10. A full split of the superadiabatic forces is shown in Fig. 18 together with the current profile, and the divergence and the curl of the velocity field.

The steady state shares the same velocity profile with flow 7 but it possesses a different density profile. The density profile depends on the $y-$coordinate and, via a coupling with the $x-$component of the velocity profile, it generates flow and structural forces along the $\hat{\mathbf{y}}$-axis, Figs. 10(e2,f2). Interestingly, the splitting into forces parallel and perpendicular to the velocity reveals that the forces $\mathbf{f}^{||}_{\text{flow}} \cdot \hat{\mathbf{y}}$, $\mathbf{f}^{\perp}_{\text{flow}} \cdot \hat{\mathbf{x}}$, $\mathbf{f}^{||}_{\text{str}} \cdot \hat{\mathbf{y}}$, and $\mathbf{f}^{\perp}_{\text{str}} \cdot \hat{\mathbf{x}}$ vanish due to the absence of flow along the $\hat{\mathbf{y}}-$axis, see Fig. 18(a2,b1,c2,d1).

IV. FINITE SIZE EFFECTS

So far we have discussed results for a square simulation box of size $H/\sigma = 5$. Although a complete finite size study is out of the scope of this paper, we have ruled out the occurrence of strong finite size effects by studying two systems (flows 9 and 10) with double the size of the simulation box, i.e. $H/\sigma = 10$ and the same overall density for which we multiply the number of particles by a factor four. The results are shown in Figs. 19 to 22.

Both flows with $H/\sigma = 10$ are related to Flow 1. Flow 9 is the same as Flow 1 but with a different box size H, c.f. Eq. (29). The shape of all superadiabatic forces is the same in both flows, compare Fig. 3 with Fig. 19 and Fig. 11 with Fig. 21. This is a further confirmation that the superadiabatic forces depend only on the shape of the density and the velocity profiles. The magnitude of the superadiabatic forces is different in both flows, which is also expected according to PFT. In the larger box (Flow 9 - $H/\sigma = 10$) the gradient of the velocity field is two times smaller than in the smaller box (Flow 1 - $H/\sigma = 5$), compare Figs. 11(e2) and 21(e2). The magnitude of the total superadiabatic forces is approximately a factor four smaller in the larger box, compare Figs. 3(d1-d2) and 19(d1-d2). The leading term in the expansion of P_t^{exc} for flow 1 is that in Eq. (12) that contains two gradient operators. Therefore, as the velocity gradient field in flow 9 is a factor two smaller than in flow 1, our PFT predicts a reduction of roughly a factor four, which is completely consistent with the simulation data.

Finally, the theoretical predictions of the superadiabatic forces presented in Figs. 19 and 21 for flow 9 have been obtained using the same transport coefficients as those for flow 1. Despite no new adjustment of the transport coefficients has been performed, the agreement between theory and simulation data is very good. The theory slightly underestimates the superadiabatic forces which might be partially due to finite size effects.

Results for flow 10 are presented in Figs. 20 and 22. Flow 10 is similar to flow 1 but doubling the frequency of the velocity field, compare Figs. 20(a1-a2) and 3(a1-a2). The magnitude of the gradient of the velocity field remains therefore the same in both flows, c.f. Figs. 11(e2) and 22(e2). Only the shape changes in a controlled manner, flow 10 is like four flows 1 replicated in a larger simulation box. Using the flow and structural transport coefficients obtained in flow 1 we are able to reproduce the superadiabatic forces in excellent agreement with those obtained in simulations, confirming again that strong finite size effects are not present.

In summary, we have shown that by custom designing the steady state of a fluid via prescribing both the density profile and the velocity profile in specific ways, one is able to specifically trigger the nonequilibrium response of the fluid. Depending on the type of flow and on the spatial inhomogeneous structure, both viscous and structural superadiabatic responses are generated. The corresponding force fields can only be fully understood on the basis of splitting into components that are parallel and perpendicular to the local flow direction.

Although we have limited the study to purely repulsive Lennard-Jones particles, superadiabatic effects are always present in nonequilibrium interacting systems. We expect the theory proposed here to reproduce the correct shape of the superadiabatic forces in systems with isotropic interactions. The flow and the structural transport coefficients will however depend on the details of the interparticle potential. Moreover, in systems with anisotropic interactions (e.g. lyotropic liquid crystals and patchy colloidal systems) both superadiabatic forces and superadiabatic torques will appear in nonequilibrium situations.

The presented methodology is highly flexible, as it allows to target specific types of nonequilibrium behaviour. Recall that all internal force fields ultimately originate from the interparticle interaction potential. Hence the classification allows to systematically address the influence of the nature of the interparticle forces, whether attractive, long-ranged etc. Furthermore, addressing the three-dimensional case is conceptually straightforward, and comes only at increased complexity of the required data analysis.

Finally, each type of superadiabatic contribution can be further split into conservative and nonconservative forces using the Helmholtz-Hodge decomposition of a vector field. The analysis of this further splitting can shed light on the intricate structure of the excess power functional that acts as a generator of the nonequilibrium internal force field.

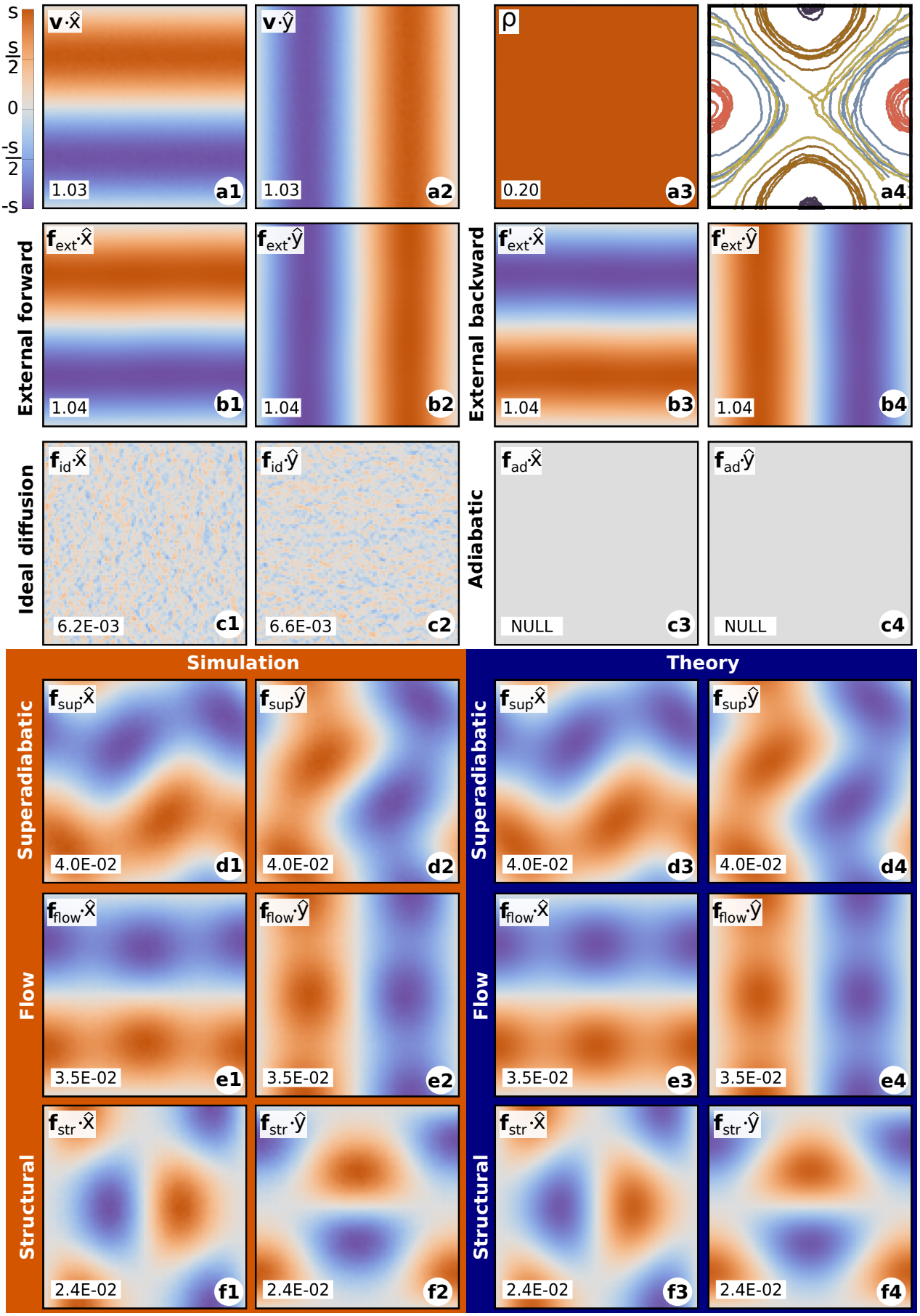

FIG. 3. Flow 1. Velocity (a1,a2) and density (a3) profiles. Illustrative trajectories calculated in absence of Brownian motion (a4). External force in the forward system (b1,b2) and in the reverse system (b3,b4). Ideal diffusion (c1,c2) and adiabatic force (c3,c4). Total superadiabatic force in simulation (d1,d2) and predicted by theory (d3,d4). Flow superadiabatic force: simulation (e1,e2), and theory (e3,e4). Structural superadiabatic force: simulation (f1,f2), theory (f3,f4).

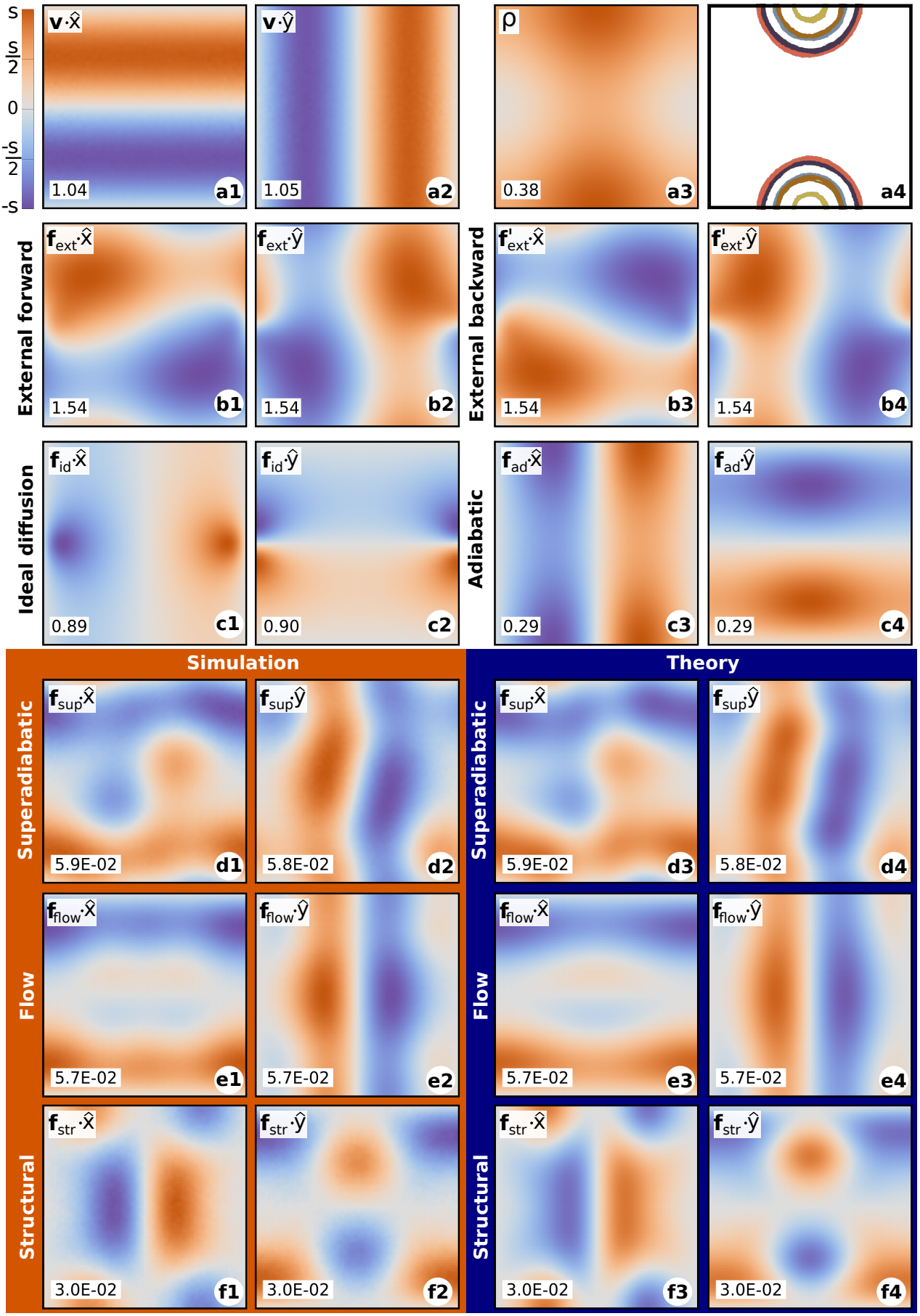

FIG. 4. Flow 2. Velocity (a1,a2) and density (a3) profiles. Illustrative trajectories calculated in absence of Brownian motion (a4). External force in the forward system (b1,b2) and in the reverse system (b3,b4). Ideal diffusion (c1,c2) and adiabatic force (c3,c4). Total superadiabatic force in simulation (d1,d2) and predicted by theory (d3,d4). Flow superadiabatic force: simulation (e1,e2), and theory (e3,e4). Structural superadiabatic force: simulation (f1,f2), theory (f3,f4).

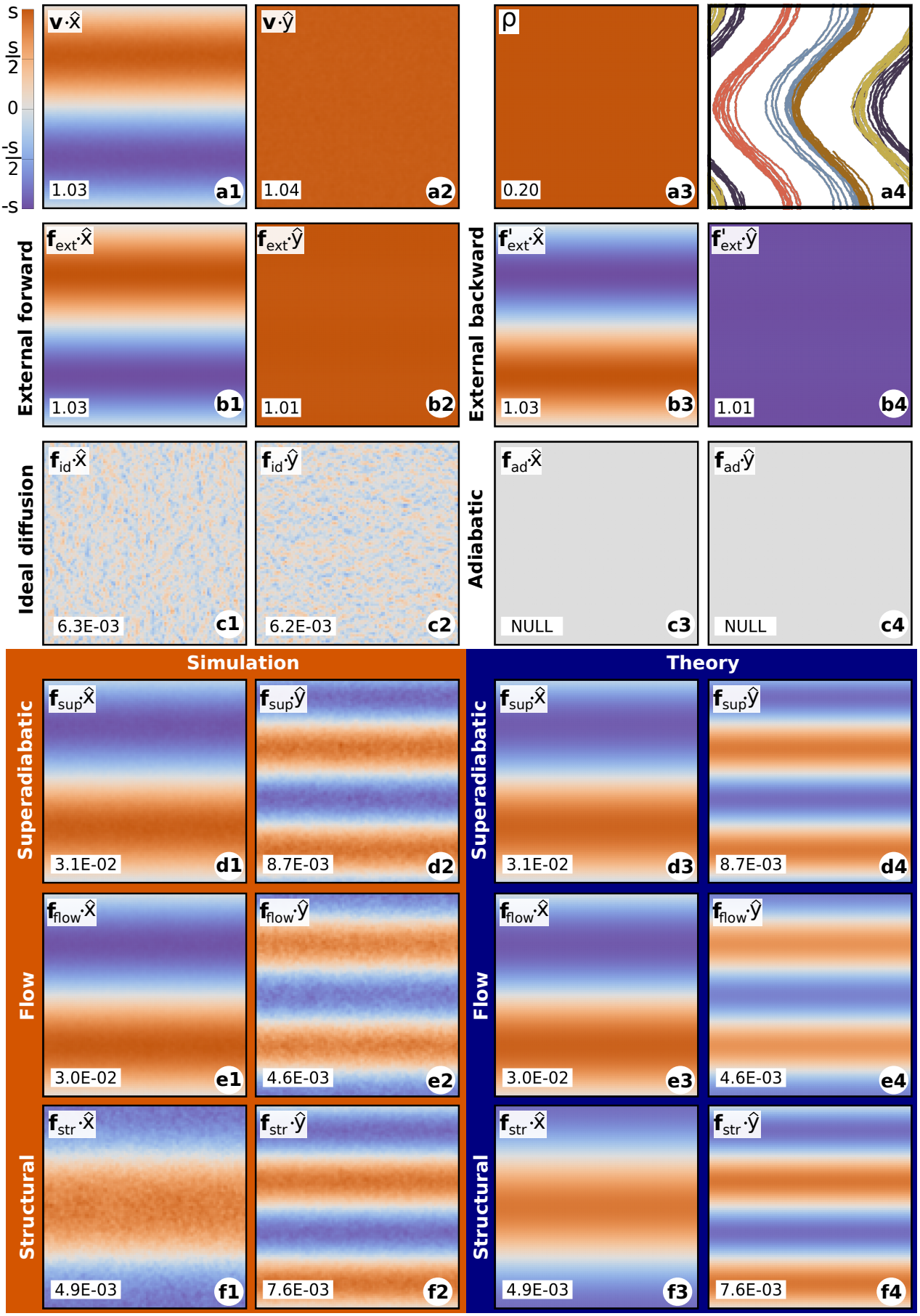

FIG. 5. Flow 3. Velocity (a1,a2) and density (a3) profiles. Illustrative trajectories calculated in absence of Brownian motion (a4). External force in the forward system (b1,b2) and in the reverse system (b3,b4). Ideal diffusion (c1,c2) and adiabatic force (c3,c4). Total superadiabatic force in simulation (d1,d2) and predicted by theory (d3,d4). Flow superadiabatic force: simulation (e1,e2), and theory (e3,e4). Structural superadiabatic force: simulation (f1,f2), theory (f3,f4).

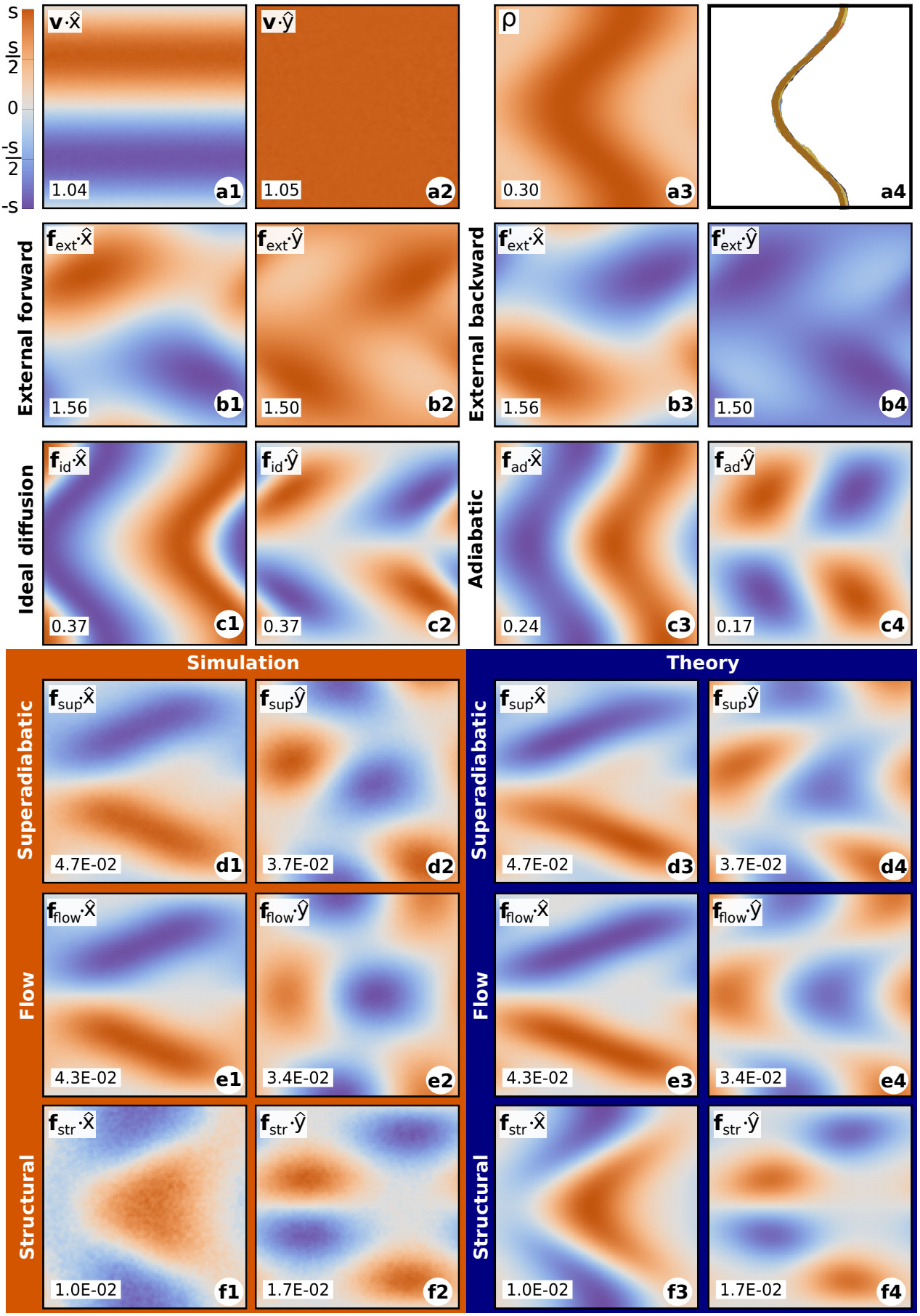

FIG. 6. Flow 4. Velocity (a1,a2) and density (a3) profiles. Illustrative trajectories calculated in absence of Brownian motion (a4). External force in the forward system (b1,b2) and in the reverse system (b3,b4). Ideal diffusion (c1,c2) and adiabatic force (c3,c4). Total superadiabatic force in simulation (d1,d2) and predicted by theory (d3,d4). Flow superadiabatic force: simulation (e1,e2), and theory (e3,e4). Structural superadiabatic force: simulation (f1,f2), theory (f3,f4).

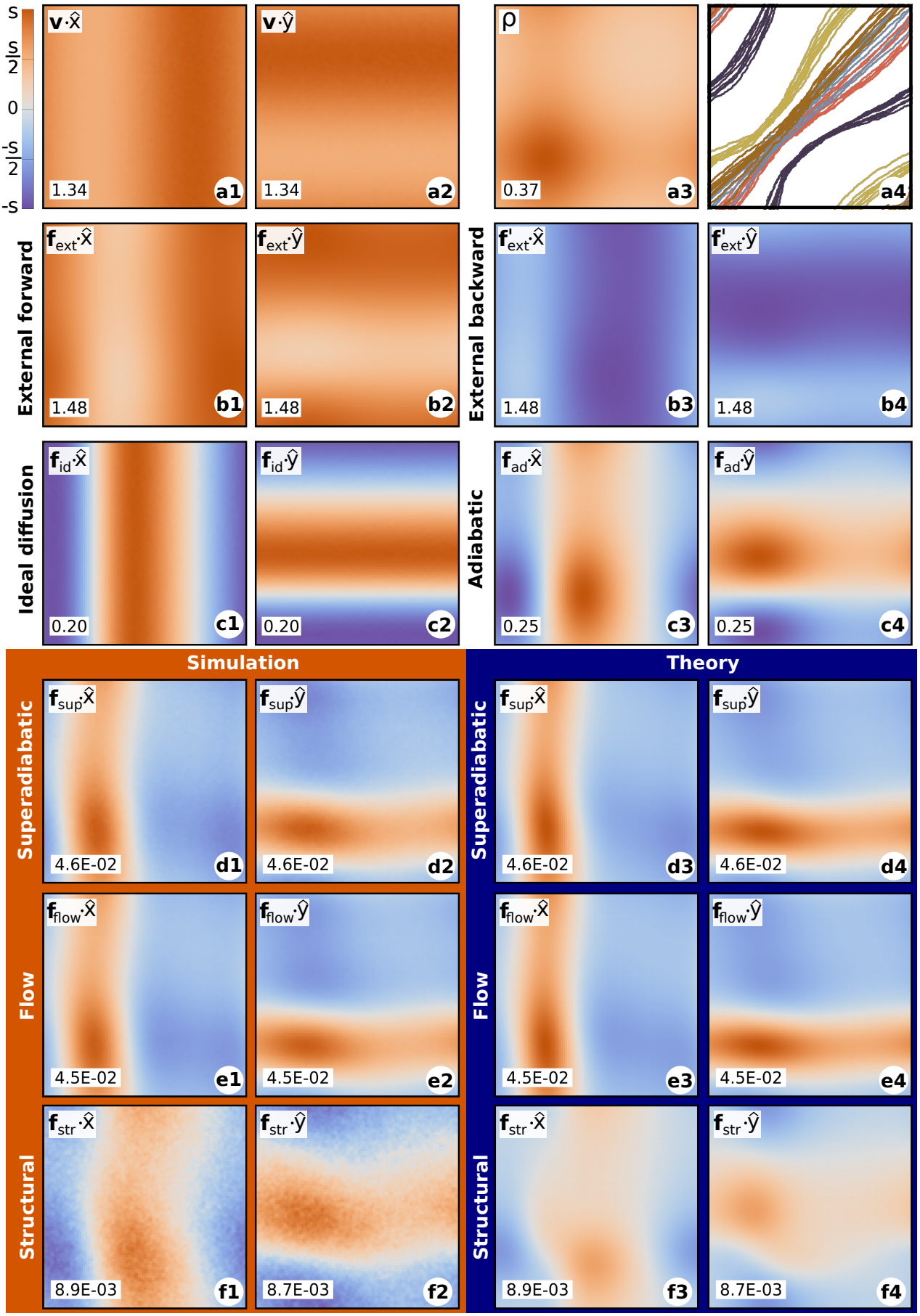

FIG. 7. Flow 5. Velocity (a1,a2) and density (a3) profiles. Illustrative trajectories calculated in absence of Brownian motion (a4). External force in the forward system (b1,b2) and in the reverse system (b3,b4). Ideal diffusion (c1,c2) and adiabatic force (c3,c4). Total superadiabatic force in simulation (d1,d2) and predicted by theory (d3,d4). Flow superadiabatic force: simulation (e1,e2), and theory (e3,e4). Structural superadiabatic force: simulation (f1,f2), theory (f3,f4).

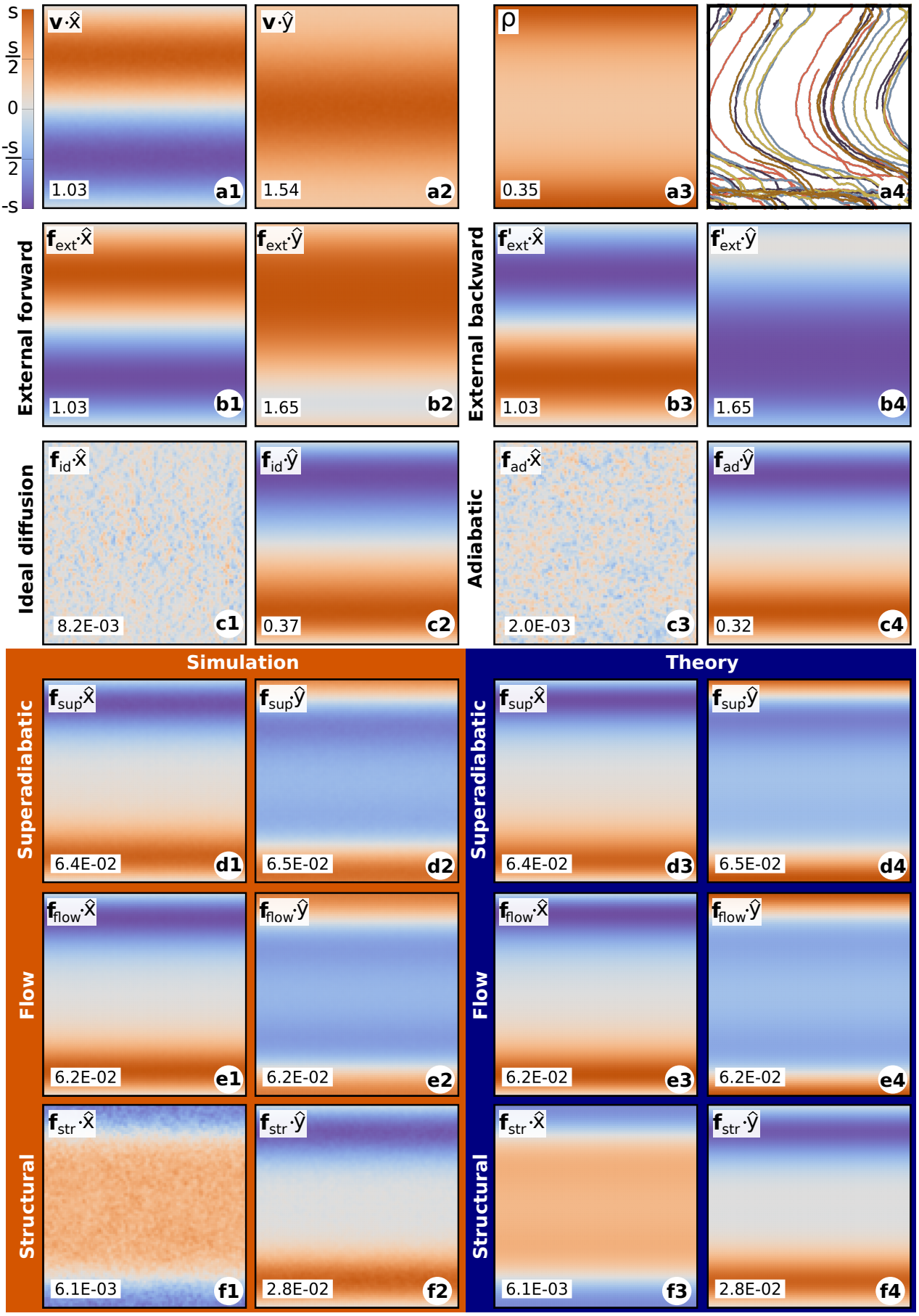

FIG. 8. Flow 6. Velocity (a1,a2) and density (a3) profiles. Illustrative trajectories calculated in absence of Brownian motion (a4). External force in the forward system (b1,b2) and in the reverse system (b3,b4). Ideal diffusion (c1,c2) and adiabatic force (c3,c4). Total superadiabatic force in simulation (d1,d2) and predicted by theory (d3,d4). Flow superadiabatic force: simulation (e1,e2), and theory (e3,e4). Structural superadiabatic force: simulation (f1,f2), theory (f3,f4).

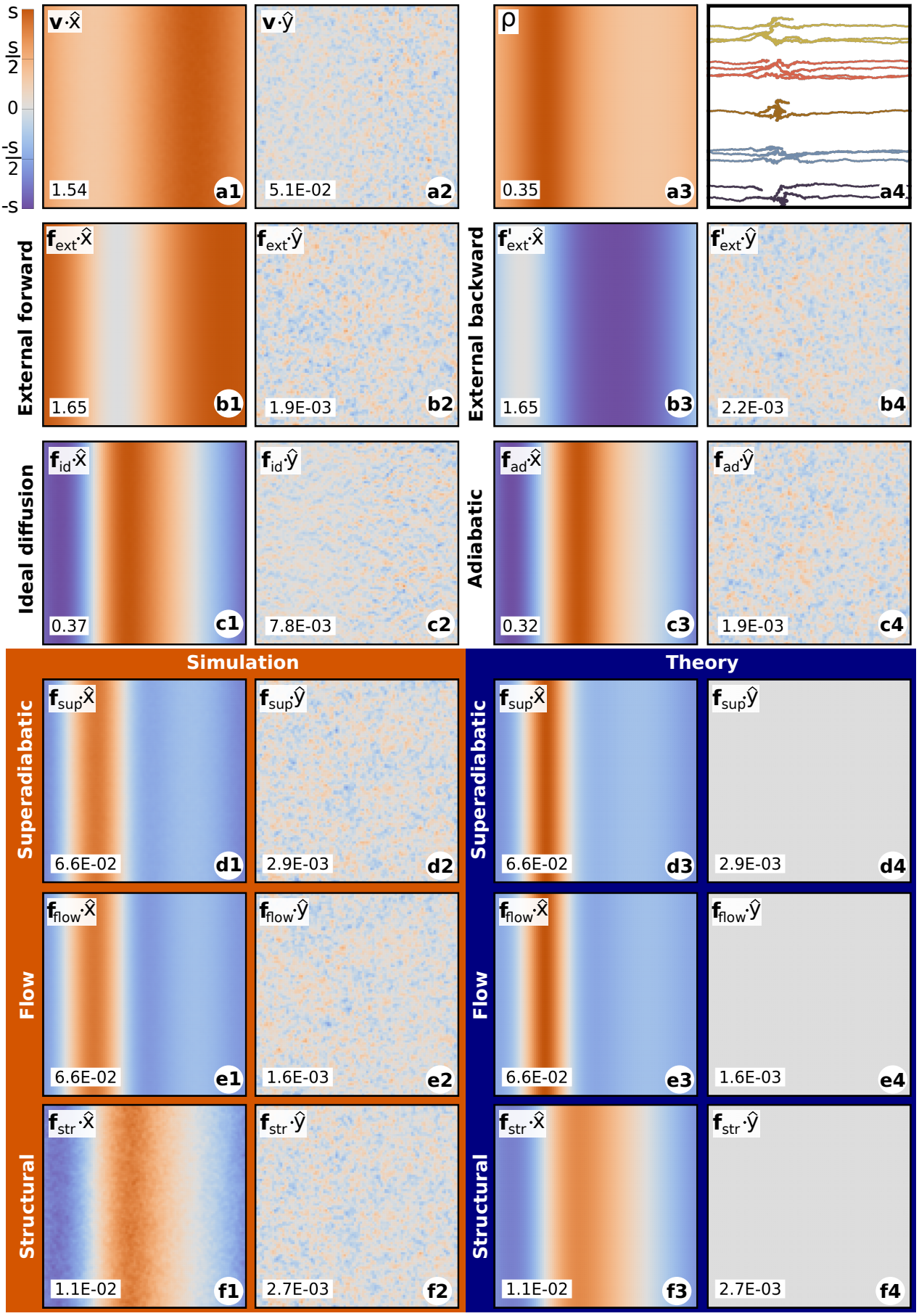

FIG. 9. Flow 7. Velocity (a1,a2) and density (a3) profiles. Illustrative trajectories calculated in absence of Brownian motion (a4). External force in the forward system (b1,b2) and in the reverse system (b3,b4). Ideal diffusion (c1,c2) and adiabatic force (c3,c4). Total superadiabatic force in simulation (d1,d2) and predicted by theory (d3,d4). Flow superadiabatic force: simulation (e1,e2), and theory (e3,e4). Structural superadiabatic force: simulation (f1,f2), theory (f3,f4).

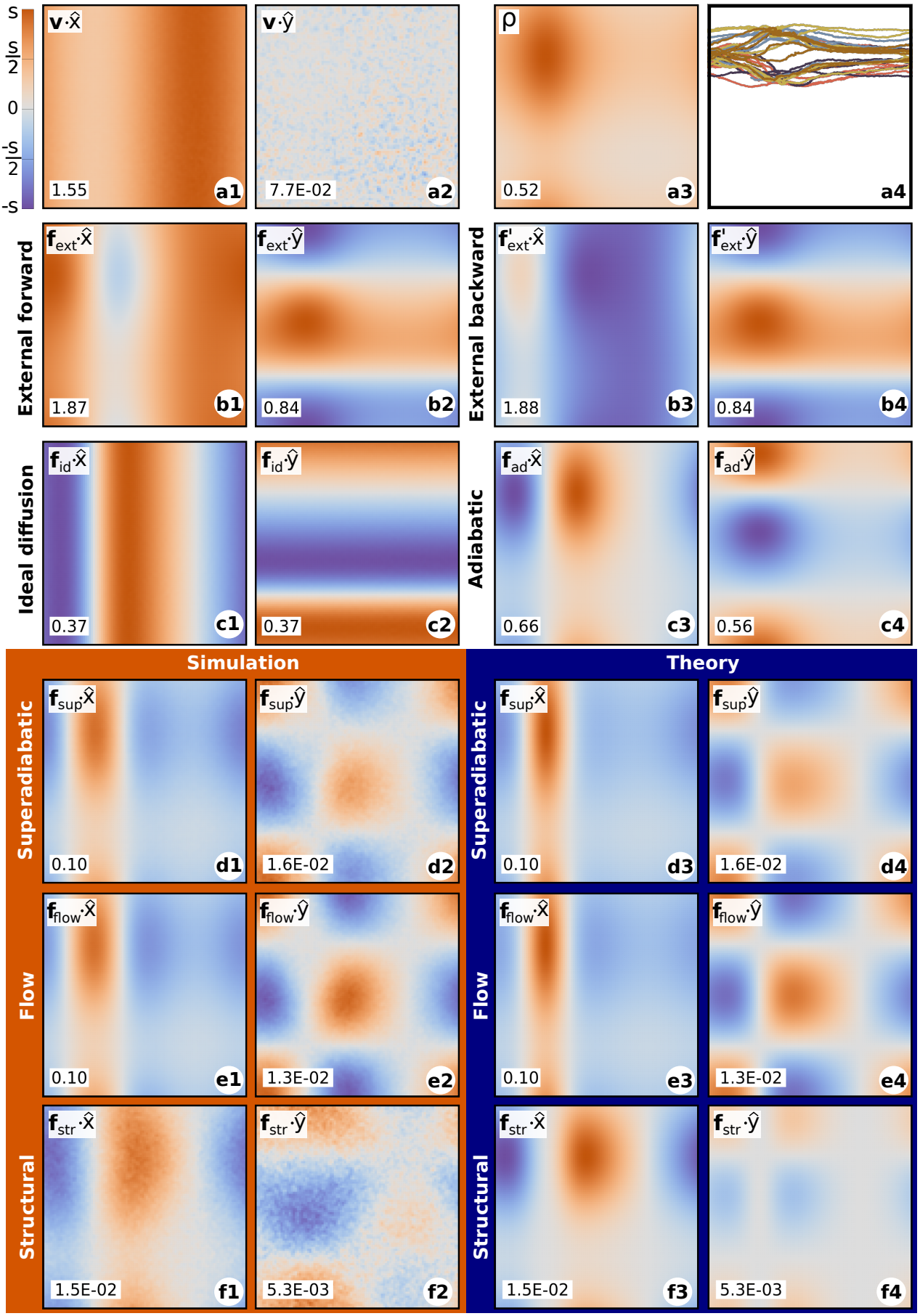

FIG. 10. Flow 8. Velocity (a1,a2) and density (a3) profiles. Illustrative trajectories calculated in absence of Brownian motion (a4). External force in the forward system (b1,b2) and in the reverse system (b3,b4). Ideal diffusion (c1,c2) and adiabatic force (c3,c4). Total superadiabatic force in simulation (d1,d2) and predicted by theory (d3,d4). Flow superadiabatic force: simulation (e1,e2), and theory (e3,e4). Structural superadiabatic force: simulation (f1,f2), theory (f3,f4).

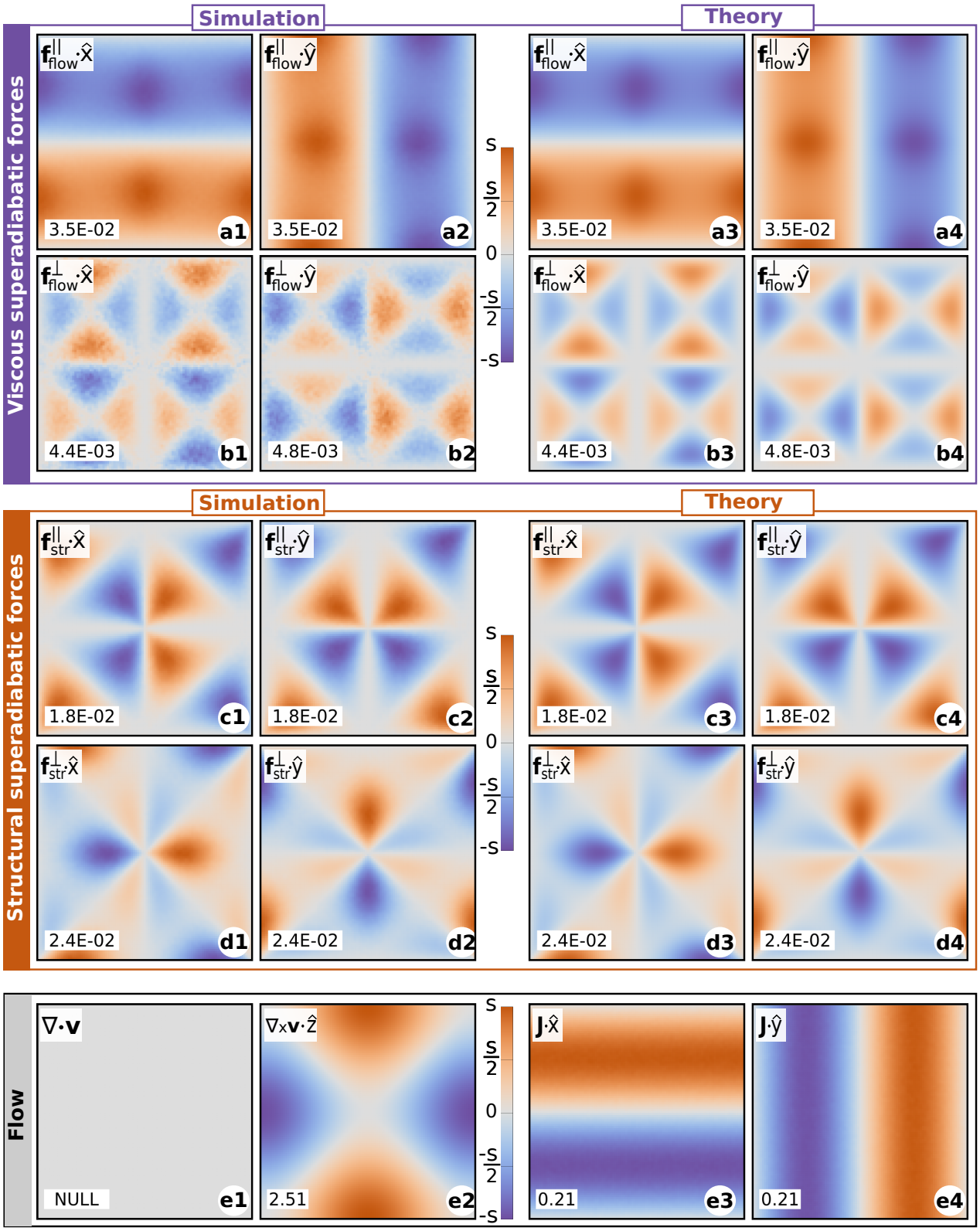

FIG. 11. Flow 1. Complete split of the superadiabatic forces according to BD simulations (left panels) and theory (right panels). (a1-a4) Flow force parallel to the flow, (b1-b4) flow force perpendicular to the flow, (c1-c4) structural force parallel to the flow, (d1-d4) structural force perpendicular to the flow. Divergence (e1) and z-component of the curl (e2) of the velocity field. Panels (e3) and (e4) display the x- and y-components of the current, respectively.

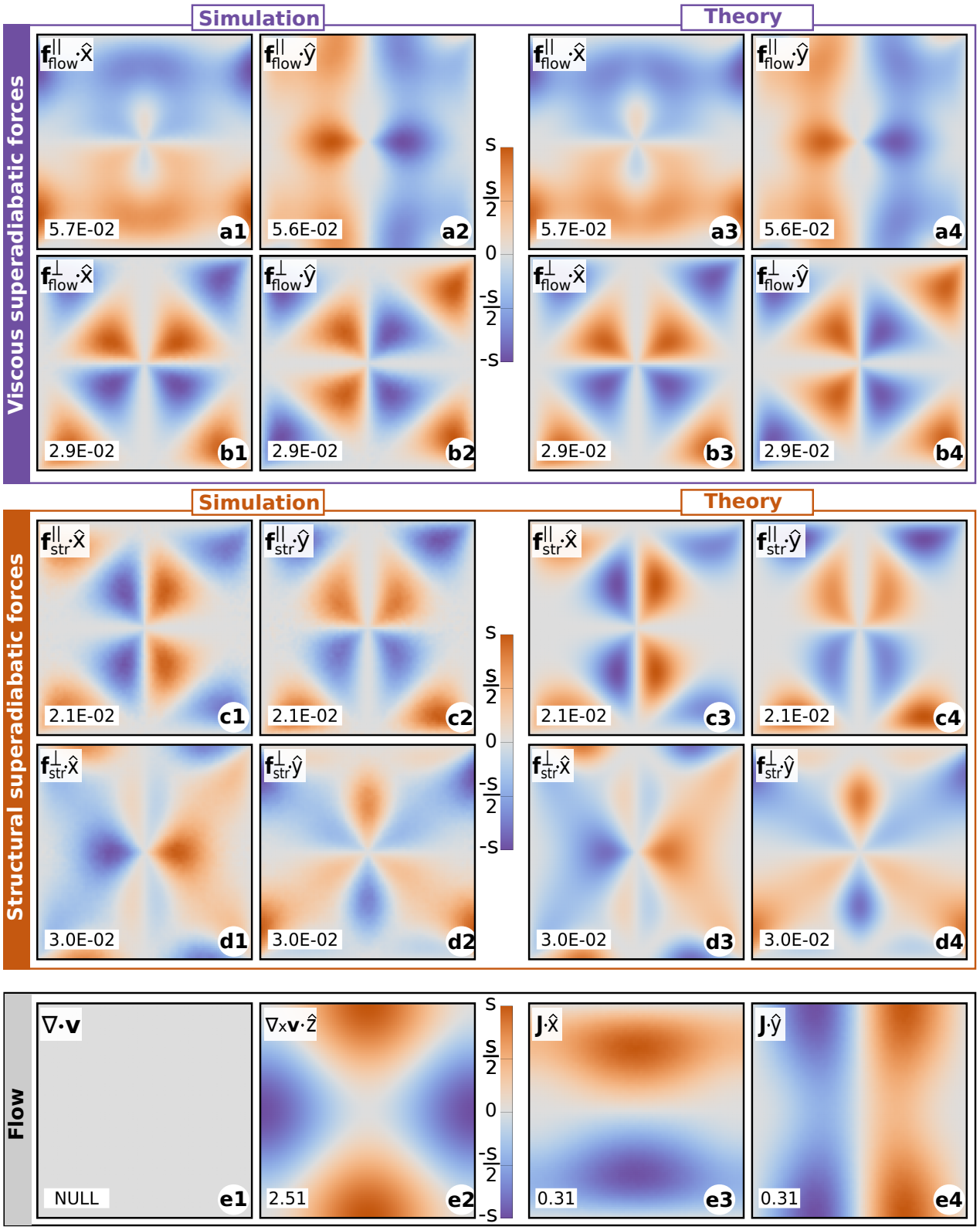

FIG. 12. Flow 2. Complete split of the superadiabatic forces according to BD simulations (left panels) and theory (right panels). (a1-a4) Flow force parallel to the flow, (b1-b4) flow force perpendicular to the flow, (c1-c4) structural force parallel to the flow, (d1-d4) structural force perpendicular to the flow. Divergence (e1) and z-component of the curl (e2) of the velocity field. Panels (e3) and (e4) display the x- and y-components of the current, respectively.

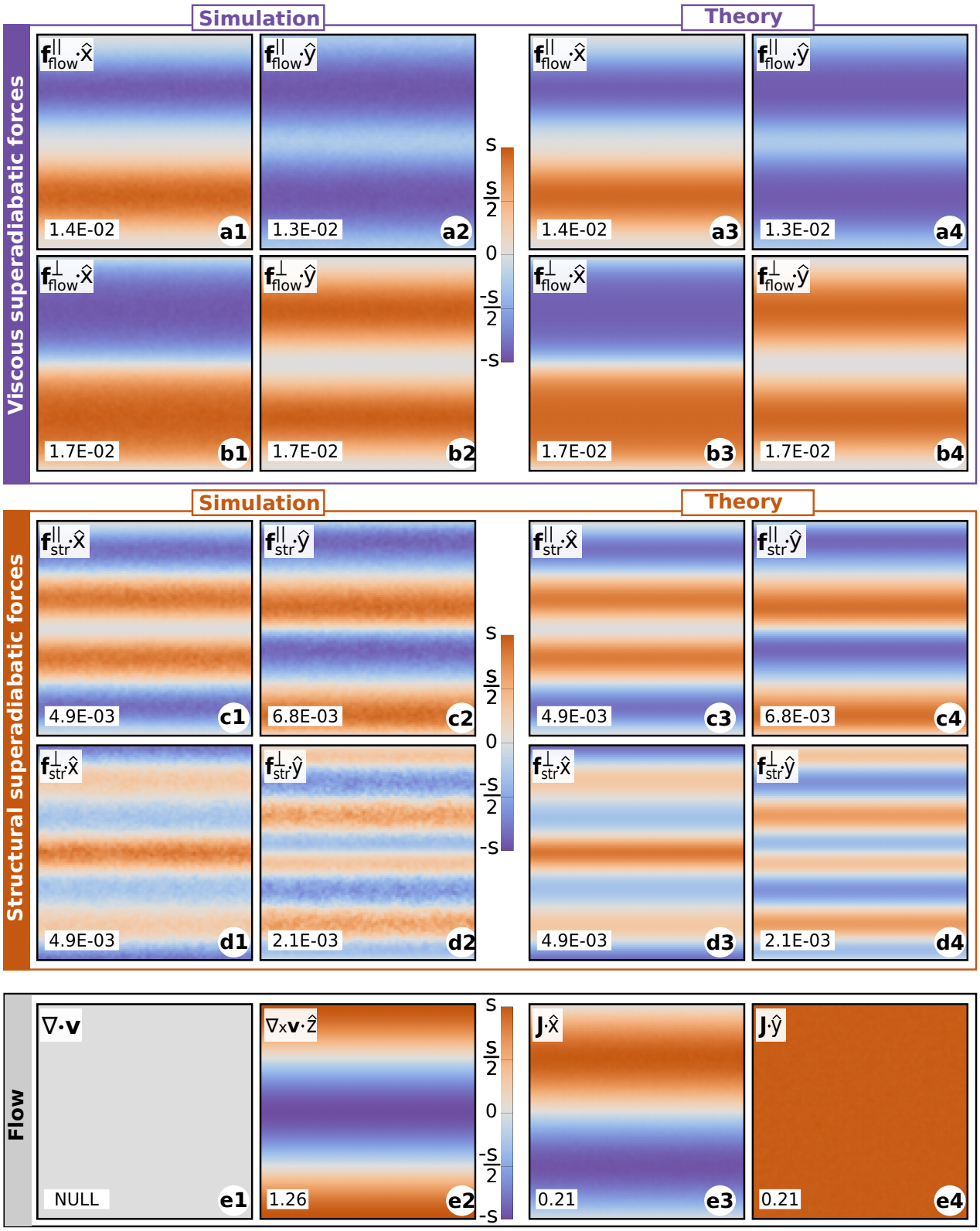

FIG. 13. Flow 3. Complete split of the superadiabatic forces according to BD simulations (left panels) and theory (right panels). (a1-a4) Flow force parallel to the flow, (b1-b4) flow force perpendicular to the flow, (c1-c4) structural force parallel to the flow, (d1-d4) structural force perpendicular to the flow. Divergence (e1) and z-component of the curl (e2) of the velocity field. Panels (e3) and (e4) display the x- and y-components of the current, respectively.

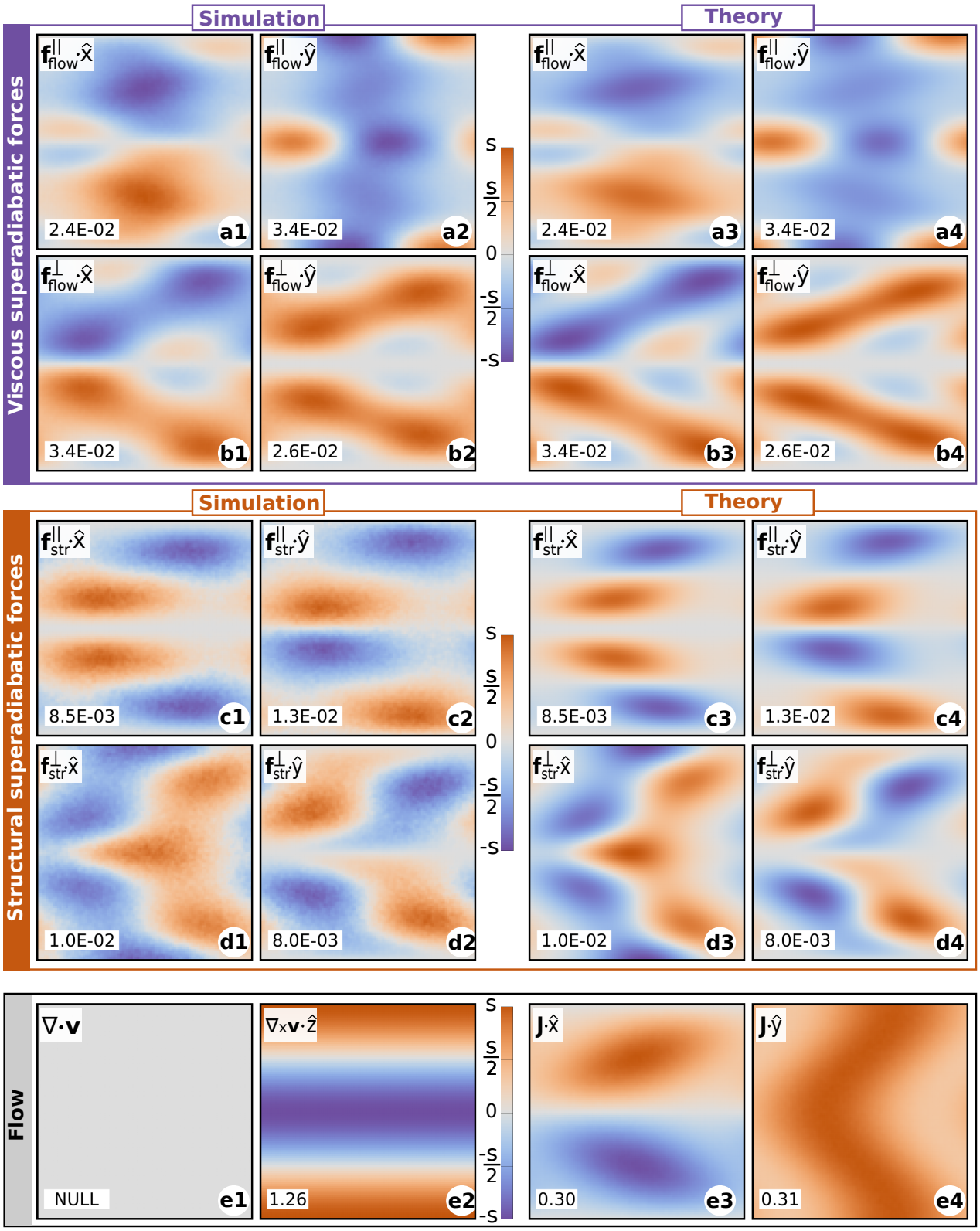

FIG. 14. Flow 4. Complete split of the superadiabatic forces according to BD simulations (left panels) and theory (right panels). (a1-a4) Flow force parallel to the flow, (b1-b4) flow force perpendicular to the flow, (c1-c4) structural force parallel to the flow, (d1-d4) structural force perpendicular to the flow. Divergence (e1) and z-component of the curl (e2) of the velocity field. Panels (e3) and (e4) display the x- and y-components of the current, respectively.

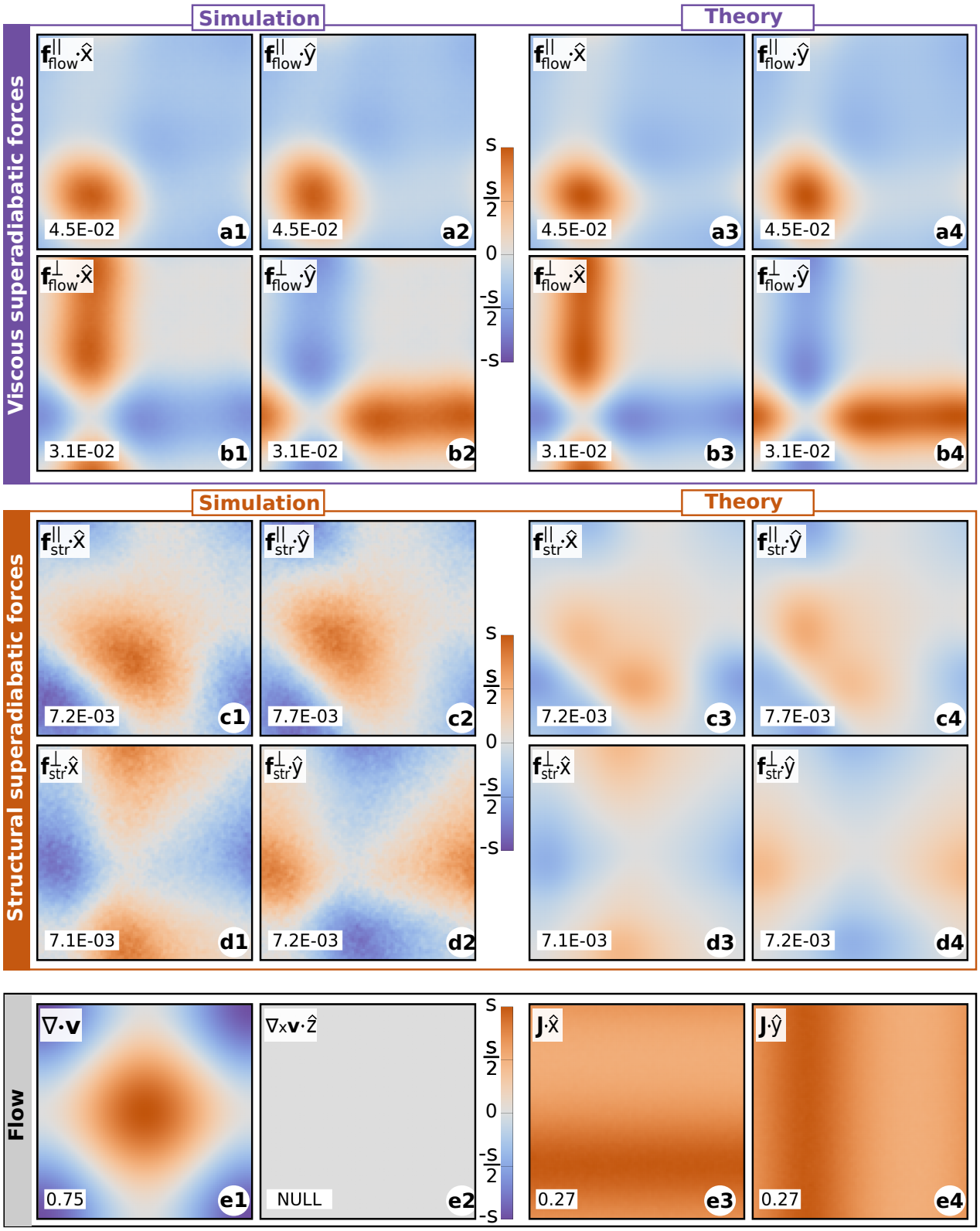

FIG. 15. Flow 5. Complete split of the superadiabatic forces according to BD simulations (left panels) and theory (right panels). (a1-a4) Flow force parallel to the flow, (b1-b4) flow force perpendicular to the flow, (c1-c4) structural force parallel to the flow, (d1-d4) structural force perpendicular to the flow. Divergence (e1) and z-component of the curl (e2) of the velocity field. Panels (e3) and (e4) display the x- and y-components of the current, respectively.

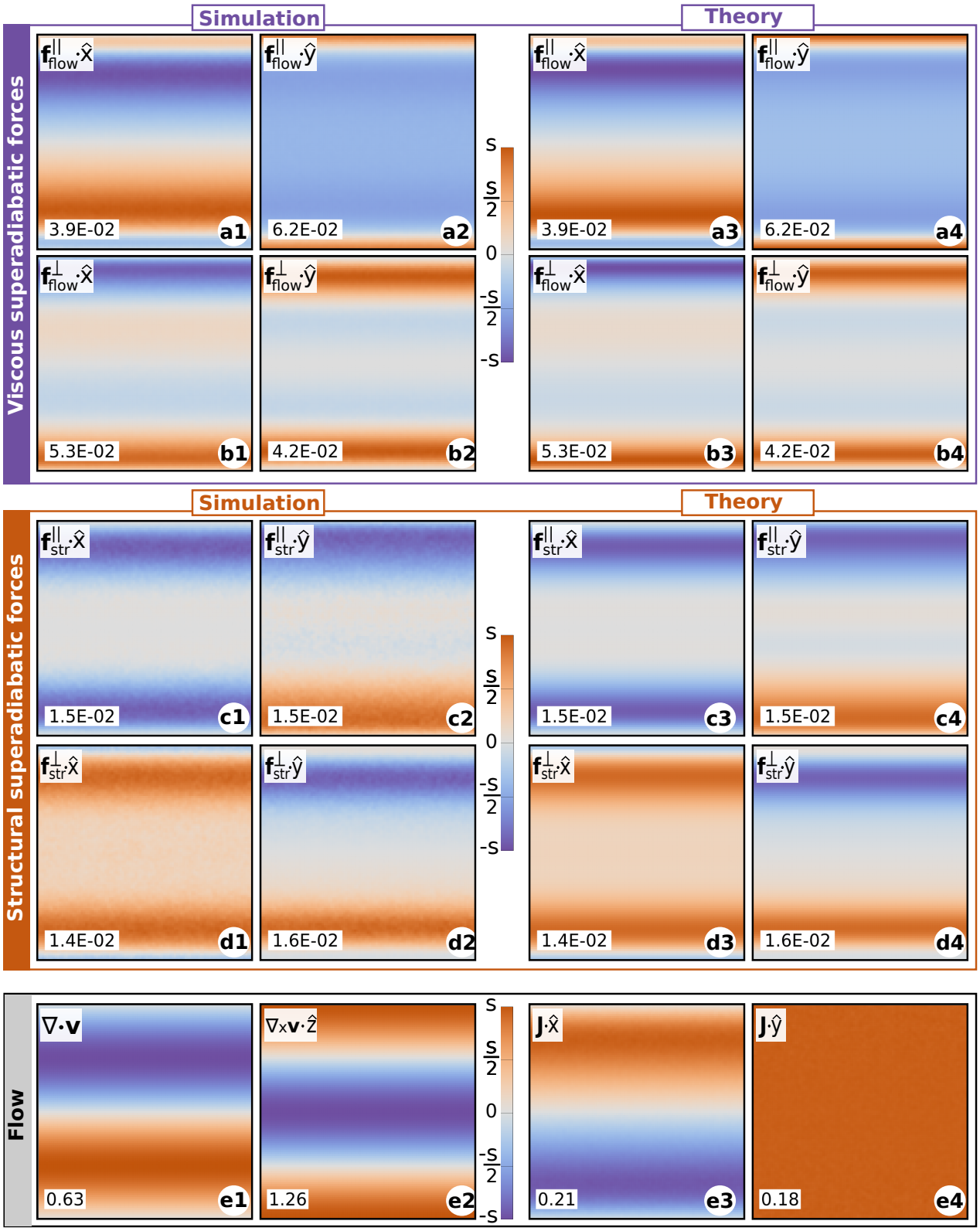

FIG. 16. Flow 6. Complete split of the superadiabatic forces according to BD simulations (left panels) and theory (right panels). (a1-a4) Flow force parallel to the flow, (b1-b4) flow force perpendicular to the flow, (c1-c4) structural force parallel to the flow, (d1-d4) structural force perpendicular to the flow. Divergence (e1) and z-component of the curl (e2) of the velocity field. Panels (e3) and (e4) display the x- and y-components of the current, respectively.

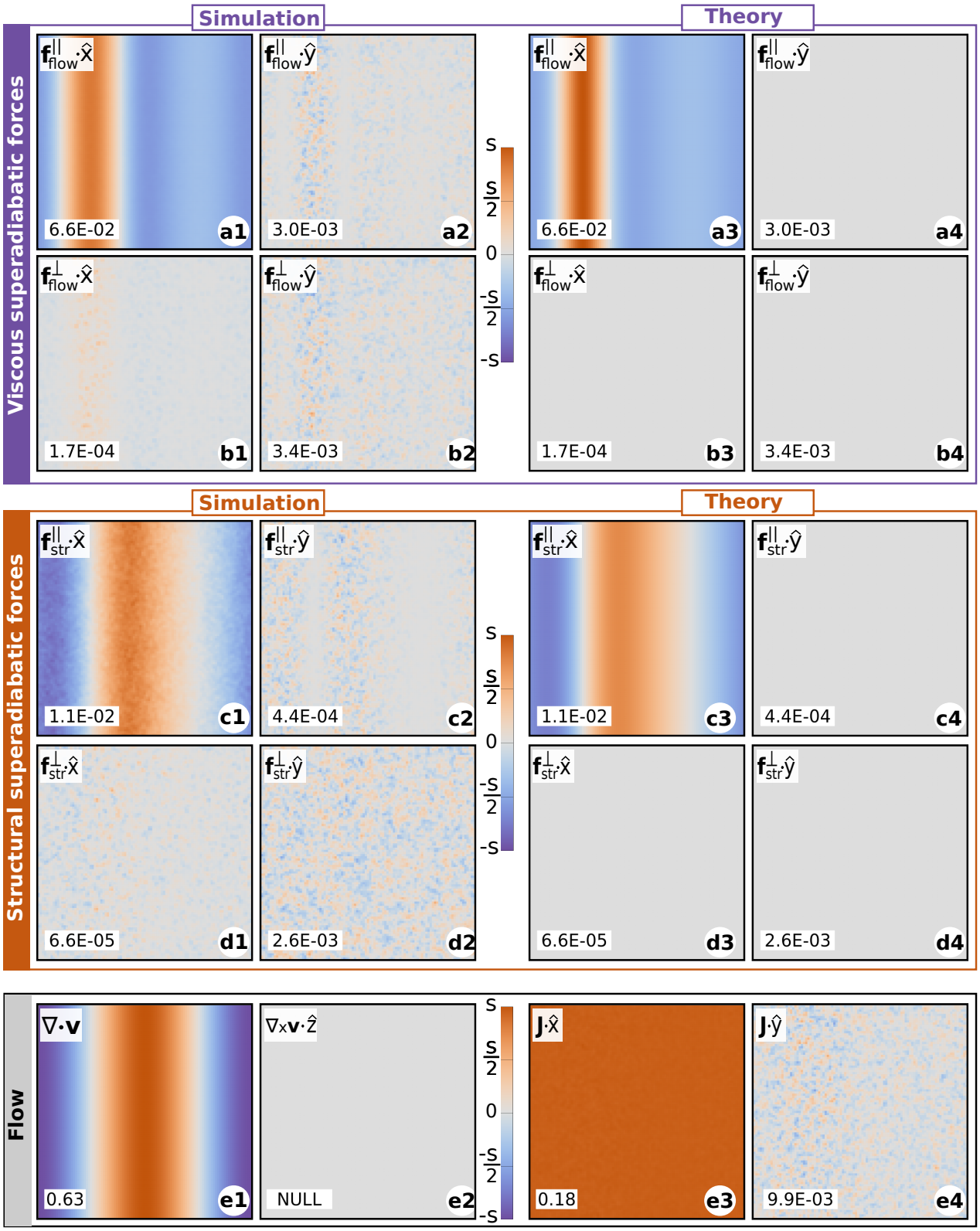

FIG. 17. Flow 7. Complete split of the superadiabatic forces according to BD simulations (left panels) and theory (right panels). (a1-a4) Flow force parallel to the flow, (b1-b4) flow force perpendicular to the flow, (c1-c4) structural force parallel to the flow, (d1-d4) structural force perpendicular to the flow. Divergence (e1) and z-component of the curl (e2) of the velocity field. Panels (e3) and (e4) display the x- and y-components of the current, respectively.

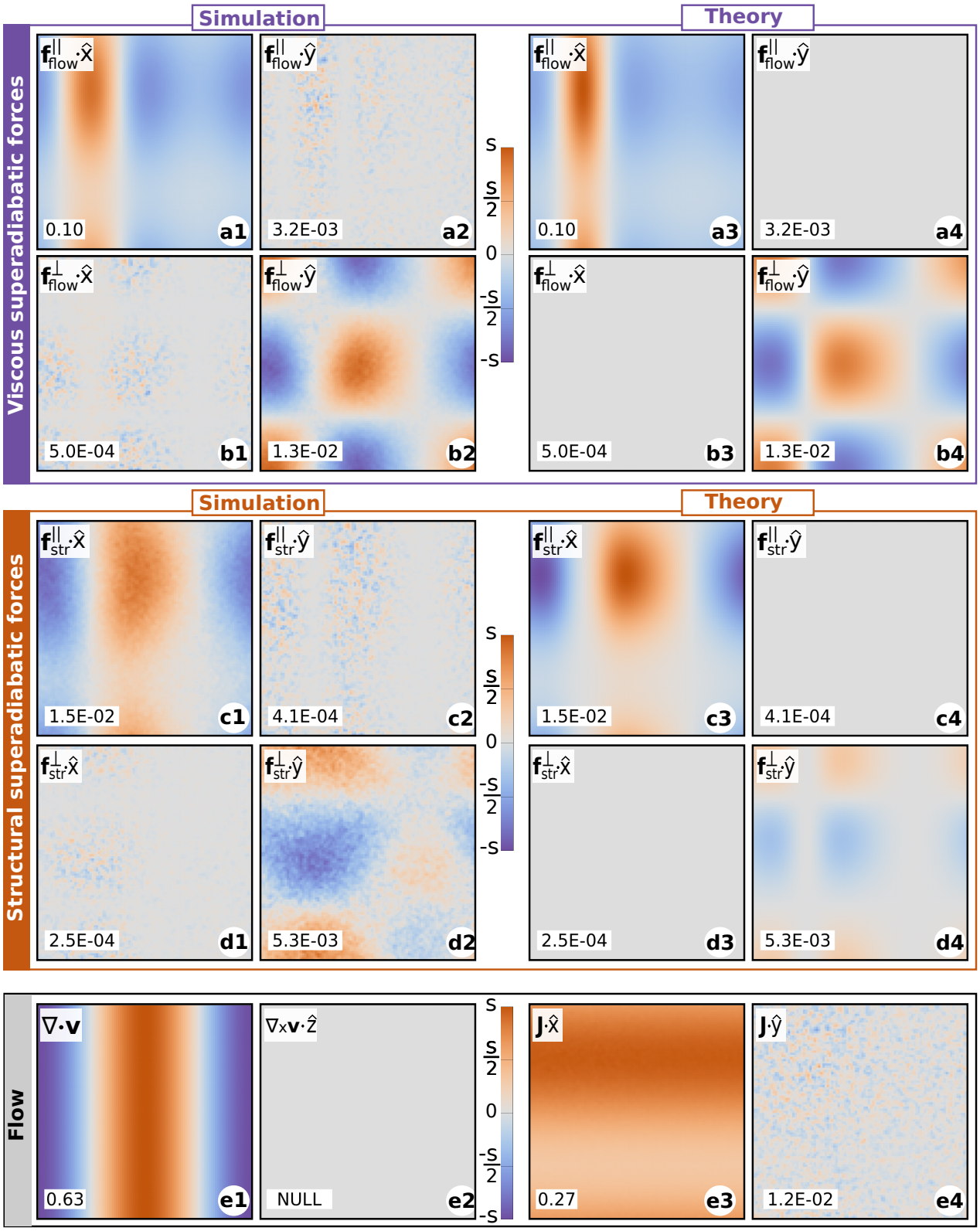

FIG. 18. Flow 8. Complete split of the superadiabatic forces according to BD simulations (left panels) and theory (right panels). (a1-a4) Flow force parallel to the flow, (b1-b4) flow force perpendicular to the flow, (c1-c4) structural force parallel to the flow, (d1-d4) structural force perpendicular to the flow. Divergence (e1) and z-component of the curl (e2) of the velocity field. Panels (e3) and (e4) display the x- and y-components of the current, respectively.

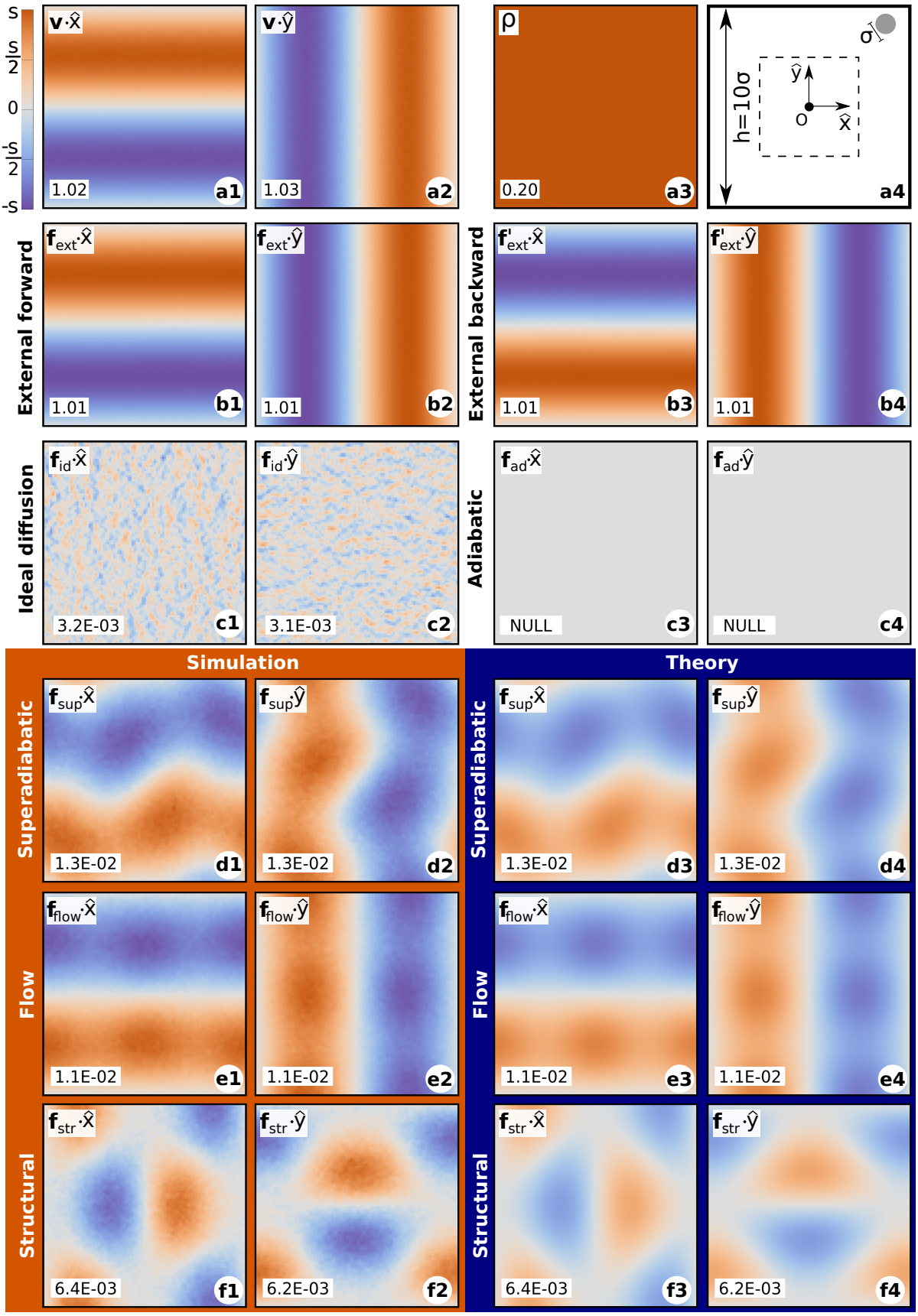

FIG. 19. Flow 9 (finite size effects). Velocity (a1,a2) and density (a3) profiles. Size of the simulation box (a4) compare to that in Flows 1-8 (dashed line). External force in the forward system (b1,b2) and in the reverse system (b3,b4). Ideal diffusion (c1,c2) and adiabatic force (c3,c4). Total superadiabatic force in simulation (d1,d2) and predicted by theory (d3,d4). Flow superadiabatic force: simulation (e1,e2), and theory (e3,e4). Structural superadiabatic force: simulation (f1,f2), theory (f3,f4).

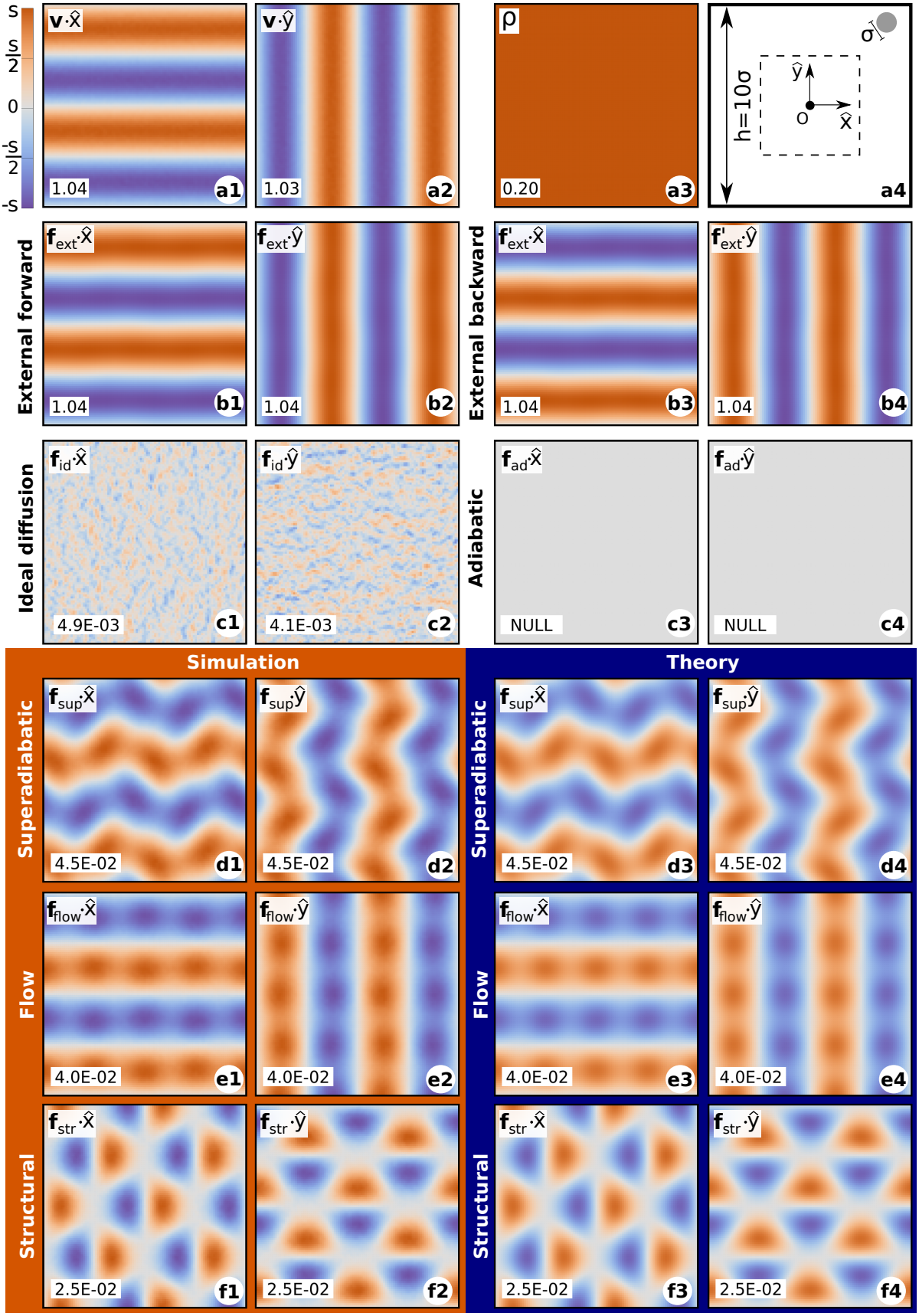

FIG. 20. Flow 10 (finite size effects). Velocity (a1,a2) and density (a3) profiles. Size of the simulation box (a4) compare to that in Flows 1-8 (dashed line). External force in the forward system (b1,b2) and in the reverse system (b3,b4). Ideal diffusion (c1,c2) and adiabatic force (c3,c4). Total superadiabatic force in simulation (d1,d2) and predicted by theory (d3,d4). Flow superadiabatic force: simulation (e1,e2), and theory (e3,e4). Structural superadiabatic force: simulation (f1,f2), theory (f3,f4).

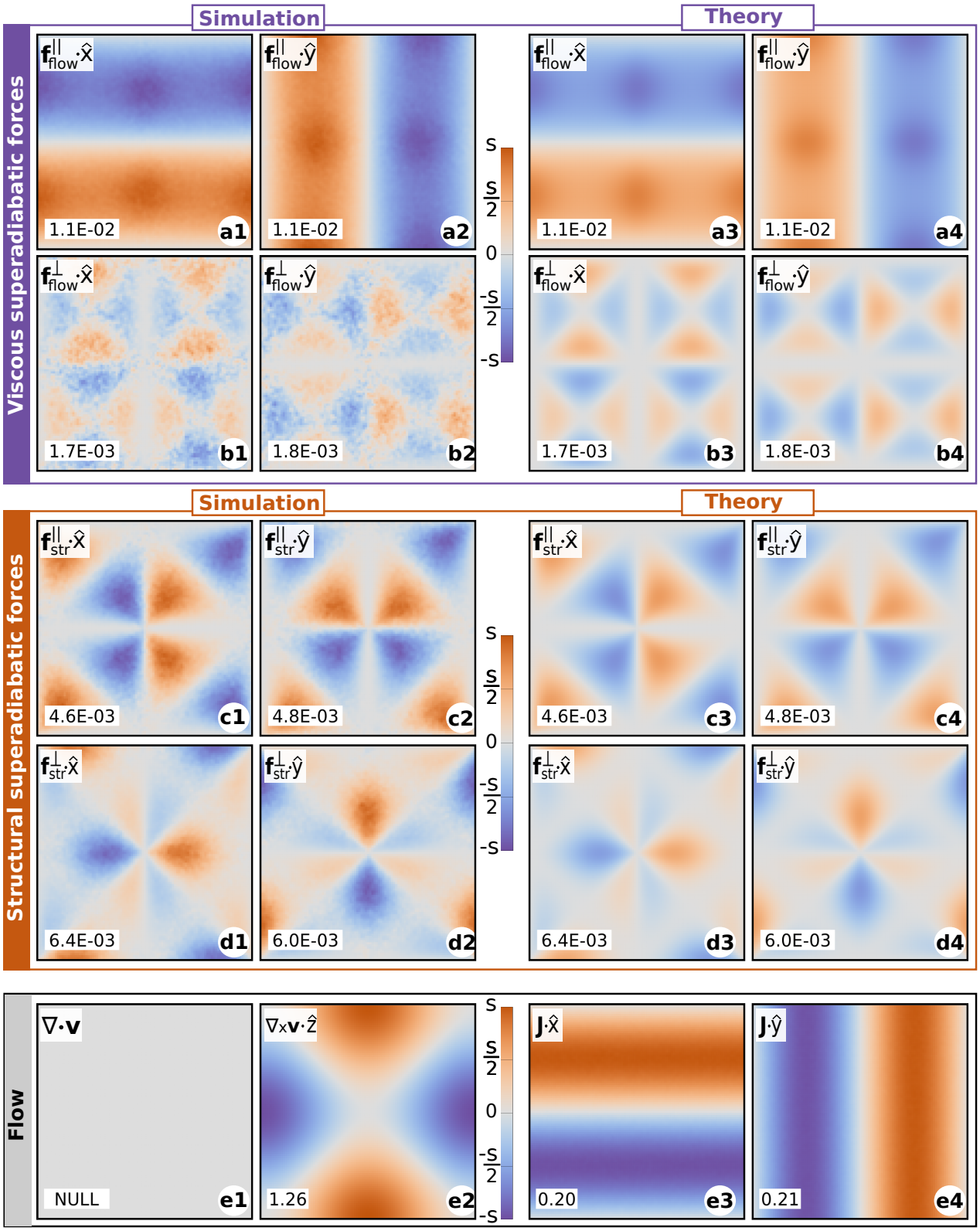

FIG. 21. Flow 9 (finite size effects). Complete split of the superadiabatic forces according to BD simulations (left panels) and theory (right panels). (a1-a4) Flow force parallel to the flow, (b1-b4) flow force perpendicular to the flow, (c1-c4) structural force parallel to the flow, (d1-d4) structural force perpendicular to the flow. Divergence (e1) and z-component of the curl (e2) of the velocity field. Panels (e3) and (e4) display the x- and y-components of the current, respectively.

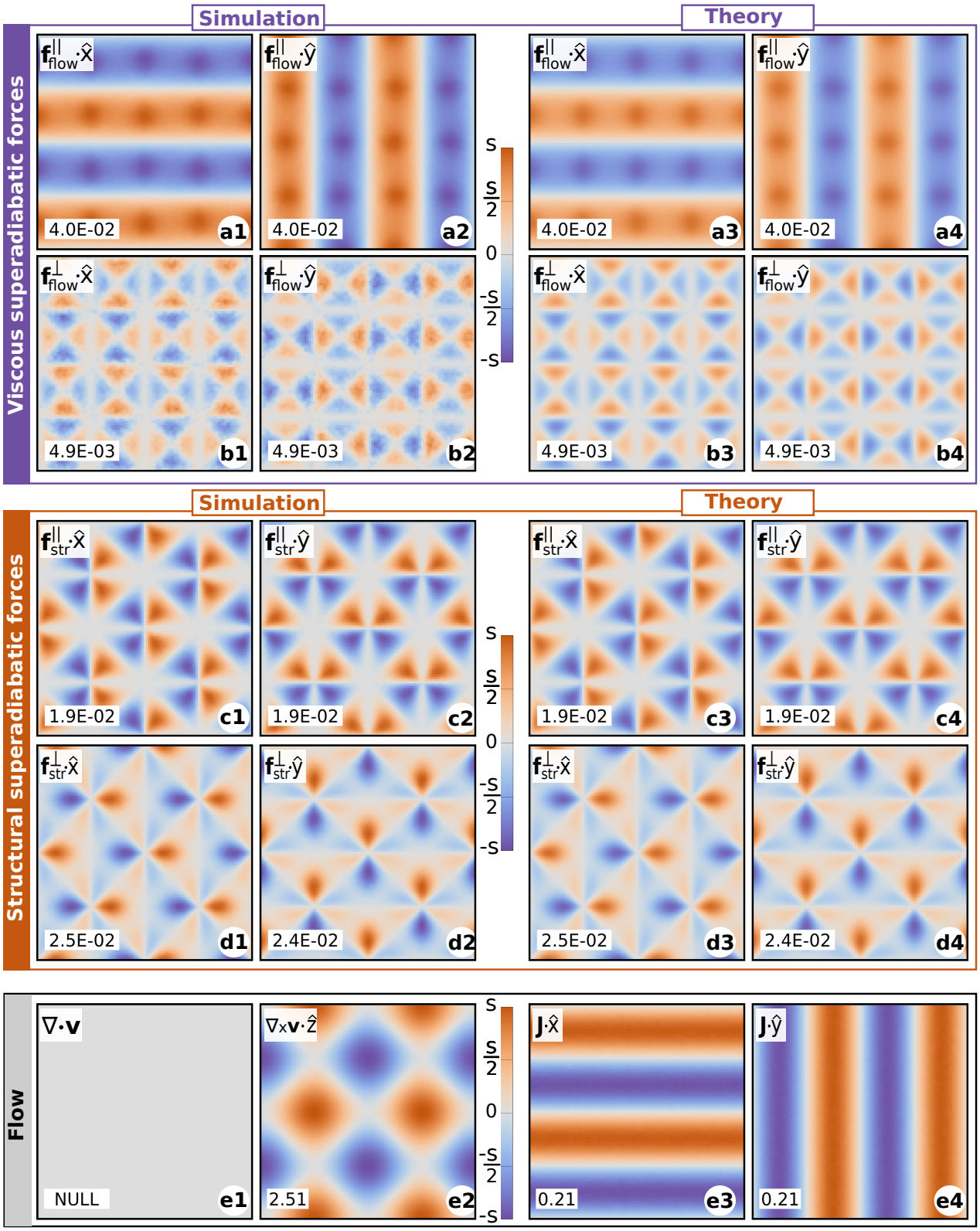

FIG. 22. Flow 10 (finite size effects). Complete split of the superadiabatic forces according to BD simulations (left panels) and theory (right panels). (a1-a4) Flow force parallel to the flow, (b1-b4) flow force perpendicular to the flow, (c1-c4) structural force parallel to the flow, (d1-d4) structural force perpendicular to the flow. Divergence (e1) and z-component of the curl (e2) of the velocity field. Panels (e3) and (e4) display the x- and y-components of the current, respectively.

[1] Daniel de las Heras, Johannes Renner, and Matthias Schmidt, "Custom flow in overdamped brownian dynamics," Phys. Rev. E **99**, 023306 (2019).

[2] John D. Weeks, David Chandler, and Hans C. Andersen, "Role of repulsive forces in determining the equilibrium structure of simple liquids," J. Chem. Phys. **54**, 5237 (1971).

[3] Nico C. X. Stuhlmüller, Tobias Eckert, Daniel de las Heras, and Matthias Schmidt, "Structural nonequilibrium forces in driven colloidal systems," Submitted (2018).

[4] R. Evans, "The nature of the liquid-vapour interface and other topics in the statistical mechanics of non-uniform, classical fluids," Advances in Physics **28**, 143–200 (1979).

[5] Matthias Schmidt and Joseph M. Brader, "Power functional theory for brownian dynamics," J. Chem. Phys. **138** (2013).

[6] Daniel de las Heras and Matthias Schmidt, "Velocity gradient power functional for brownian dynamics," Phys. Rev. Lett. **120**, 028001 (2018).